

1  
2  
3  
4  
5  
6  
7  
8  
9  
10  
11  
12  
13  
14  
15  
16  
17  
18

**Radiative sensitivity quantified by a new set of radiation flux kernels based on the ERA5 reanalysis**

Han Huang, Yi Huang

Department of Atmospheric and Oceanic Sciences, McGill University, Montreal, Canada

Corresponding Authors:

Han Huang, han.huang2@mcgill.ca (ORCID: 0000-0002-9143-6453),  
Yi Huang, yi.huang@mcgill.ca (ORCID: 0000-0002-5065-4198)

19 **Abstract**

20

21 Radiative sensitivity, i.e., the response of the radiative flux to climate perturbations, is essential  
22 to understanding climate variability. The sensitivity kernels computed by radiative transfer  
23 models have been broadly used for assessing the climate forcing and feedbacks for global  
24 warming. As these assessments are largely focused on the top of atmosphere (TOA) radiation  
25 budget, less attention has been paid to the surface radiation budget or the associated surface  
26 radiative sensitivity kernels. Based on the fifth generation European Center for Medium-Range  
27 Weather Forecasts (ERA5) atmospheric reanalysis, we produce a new set of radiative kernels for  
28 both the TOA and surface radiative fluxes, which is made available at  
29 <http://dx.doi.org/10.17632/vmg3s67568.2> (Huang and Huang, 2023). By comparing with other  
30 published radiative kernels, we find that the TOA kernels are generally in agreement in terms of  
31 global mean radiative sensitivity and analyzed overall feedback strength. The unexplained  
32 residual in the radiation closure tests is found to be generally within 10%, no matter which kernel  
33 dataset is used. The uncertainty in the TOA feedbacks caused by inter-kernel differences, as  
34 measured by the standard deviation of the global mean feedback parameter value is much smaller  
35 than the inter-climate model spread of the feedback values. However, we find relatively larger  
36 discrepancies in the surface kernels. The newly generated ERA5 kernel outperforms many other  
37 datasets in closing the surface energy budget, achieving a radiation closure comparable to the  
38 TOA feedback decomposition, which affirms the validity of kernel method for the surface  
39 radiation budget analysis. In this paper, we provide a detailed description on how ERA5 kernels  
40 are generated and considerations to ensure proper use of them in feedback quantifications.

41

42

43

## 44 1. Introduction

45

46 Radiative kernels measure the sensitivity of radiative fluxes to the perturbation of feedback  
47 variables, such as temperature, water vapor, albedo and cloud (e.g., Soden and Held, 2006;  
48 Huang et al., 2007; Shell et al., 2008; Previdi, 2010; Zelinka et al., 2012; Block and Mauritsen,  
49 2013; Yue et al., 2016; Huang et al., 2017; Pendergrass et al., 2018; Thorsen et al., 2018; Kramer  
50 et al., 2019b; Smith et al., 2020). Compared to the partial radiative perturbation method (e.g.,  
51 Wetherald and Manabe, 1988), which is precise but computationally expensive, the kernel  
52 method deploys a set of precalculated radiative kernels with simple arithmetic multiplications in  
53 feedback quantification and thus is computationally highly efficient, which has greatly facilitated  
54 the analysis of radiative feedbacks in global climate models (GCM) (e.g., Soden et al., 2008;  
55 Jonko et al., 2012; Vial et al., 2013; Zhang and Huang, 2014; Soden and Held, 2006; Dong et al.,  
56 2020; Zelinka et al., 2020; Chao and Dessler, 2021), as well as in observations (e.g., Dessler,  
57 2010; Kolly and Huang, 2018; Zhang et al., 2019; Huang et al., 2021a). These analyses have  
58 helped dissect and understand the climate sensitivity differences among the GCMs, such as those  
59 in Coupled Model Intercomparison Projects, CMIP5 (Taylor et al., 2012) and CMIP6 (Eyring et  
60 al., 2016). For example, Zelinka et al. (2020) attributed the higher climate sensitivity in the  
61 CMIP6 models to their more positive extratropical cloud feedback. The kernel-enabled feedback  
62 analyses have also provided insights in the energetics of the climate variations such as the El  
63 Nino and Southern Oscillation (ENSO, e.g., Dessler et al., 2010; Kolly & Huang 2018; Huang et  
64 al. 2021a), the Madden-Julian Oscillation (MJO, e.g., Zhang et al. 2019) and the Arctic sea ice  
65 interannual variability (e.g., Huang et al., 2019), despite the approximation nature of the kernel  
66 method and the known limits of its accuracy (e.g., Colman and Mcavaney, 1997; Huang and  
67 Huang, 2021).

68 Multiple sets of radiative kernels have been developed to date, using different radiation  
69 codes and based on different atmospheric state datasets ranging from GCMs to global reanalysis  
70 and satellite datasets, for both non-cloud variables (e.g., Soden and Held, 2006; Shell et al.,  
71 2008; Huang et al., 2017; Thorsen et al., 2018; Bright and O'halloran, 2019; Donohoe et al.,  
72 2020) and cloud properties (e.g., Zelinka et al., 2012; Zhou et al., 2013; Yue et al., 2016; Zhang  
73 et al., 2021; Zhou et al., 2022). As the conventional feedback analyses are mostly concerned with  
74 the radiation energy budget change at the TOA, most existing kernels have been developed and  
75 tested to address that need, i.e., to measure the feedback contributions to the TOA radiation  
76 changes. Although the radiative sensitivity depends on the atmospheric states as well as the  
77 radiative transfer codes used to compute the kernel values (e.g., Collins et al., 2006; Huang and  
78 Wang, 2019; Pincus et al., 2020), it has been noted that the global mean TOA feedback  
79 quantification is insensitive to which kernel dataset is used, as the diagnosed feedback values are  
80 close to each other when measured by different kernel datasets (e.g., Soden et al., 2008; Jonko et  
81 al., 2012; Vial et al., 2013). However, as there is increasing interest in regional climate change  
82 and associated feedback (e.g., Kolly and Huang, 2018; Huang et al., 2019; Zhang et al. 2019), it  
83 becomes important to know how the kernels (dis)agree at regional scales. The generation of the  
84 global radiative kernels usually requires radiative transfer computation based on a large number  
85 of instantaneous atmospheric profiles. Due to this computational cost, many kernel datasets are  
86 generated based on the atmospheric data from an arbitrary calendar year. Given the known  
87 interannual climate differences, e.g., between El Niño to La Niña years, this calls into question  
88 whether the kernels may differ in important ways for regional feedback assessments.

89 On the other hand, fewer feedback studies have addressed the surface radiation budget,  
90 although its importance has been recognized for such problems as the precipitation change  
91 (Previdi, 2010; Pendergrass and Hartmann, 2014; Myhre et al., 2018) and oceanic energy  
92 transport (e.g., Zhang and Huang, 2014; Huang et al., 2017). The surface budget analysis  
93 requires the use of surface kernels, which are not always available from the published kernel  
94 datasets. Few of them have been subject to inter-comparisons or rigorous validation. As  
95 explained below in this paper, the computation and use of them require different care than the  
96 TOA kernels. Possibly due to the lack of such recognition, there exist considerable discrepancies  
97 between the existing surface kernels and some surface budget-centered analyses reported  
98 alarmingly large non-closure in their radiation budget analyses (e.g., Vargas Zeppetello et al.,  
99 2019), calling into question the validity of kernel method for surface radiation budget analysis.  
100 Hence, we are motivated to examine the radiative sensitivity quantified by different kernels,  
101 especially for the surface budget.

102 In this work, we produce a new set of radiative kernels for both the TOA and surface  
103 radiation fluxes based on the fifth generation European Center for Medium-Range Weather  
104 Forecasts atmospheric reanalysis (ERA5, Hersbach et al., 2020), which demonstrates superior  
105 accuracy in the quantification of various atmospheric states, and document the key  
106 considerations in the kernel computation procedure. We intercompare the kernels computed from  
107 ERA5 to the other previously generated ones, and investigate the interannual variation of the  
108 kernel values due to their atmospheric state dependency. In addition, applying a selected sets of  
109 kernels to analyzing the feedback in the CMIP6 models, we intercompare the discrepancies in  
110 quantified feedbacks across the GCMs and across different kernels.

111

112

## 113 **2. Construction of ERA5 radiative kernels**

114

### 115 **2.1 Radiative transfer model and atmospheric dataset**

116

117 We use the GCM version of the rapid radiative transfer model (RRTMG) (Mlawer et al.,  
118 1997) to calculate the radiative kernels. RRTMG conducts radiative transfer calculations in 16  
119 longwave (LW) spectral bands and 14 shortwave (SW) bands. The accuracy of this model has  
120 been extensively validated against the line-by-line calculations (e.g., Collins et al, 2006).

121 Input data required by RRTMG, including surface pressure, skin temperature, air  
122 temperature, water vapor, albedo, ozone concentration, cloud fraction, cloud liquid water content  
123 and cloud ice content, are taken from the instantaneous (as opposed to monthly mean) data of the  
124 ERA5 reanalysis, with a horizontal resolution of 2.5 degree by 2.5 degree and 37 vertical  
125 pressure levels between 1 hPa and 1000 hPa. To ensure the accuracy of radiative kernels in upper  
126 atmosphere (Smith et al., 2020), we patch five layers of the U.S. standard profile above 1 hPa in  
127 the LW calculations. Other required input variables, such as the effective radii of cloud liquid  
128 droplet and ice crystal are taken from the 3-hourly synoptic TOA and surface fluxes and cloud  
129 product of the Clouds and Earth's Radiant Energy System (CERES) (Doelling et al., 2013) with  
130 a horizontal resolution of 1 degree and then interpolated to the same resolution as the ERA5 data  
131 (2.5 degree). A random cloud overlapping scheme is used in our all-sky calculation. Sensitivity  
132 tests have been conducted to determine the necessary temporal sampling for a proper  
133 representation of the diurnal cycle and 6-hourly and 3-hourly instantaneous profiles are adopted

134 for LW and SW radiative transfer calculations, respectively, to limit the root mean squared error  
135 of the computed diurnal mean flux biases to less than one percent.

136  
137

## 138 **2.2 Radiative kernel computation**

139

140 Radiative kernels in essence measure the change of radiative flux to unit perturbation of  
141 atmospheric variables, i.e.,  $\frac{\partial R}{\partial X}$ , where  $R$  is either the upwelling irradiance flux at the TOA or  
142 upwelling/downwelling irradiance flux at the surface;  $X$  represents the aforementioned feedback  
143 variables;  $K_X$  is the radiative kernel of variable  $X$ . Note that for each radiative flux,  $K_X$  varies  
144 with the time, geographic and vertical locations of the perturbed variable and is in general a 4-  
145 dimensional (4-D) data array. Note also that all radiative fluxes and kernel values are defined as  
146 downward positive.

147 Following the previous studies, we compute non-cloud radiative kernels including the LW  
148 kernels of surface temperature ( $T_s$ ), air temperature ( $T_a$ ), and water vapor ( $WV LW$ ), and the SW  
149 kernels of surface albedo ( $ALB$ ) and water vapor ( $WV SW$ ). To calculate the kernels, we use the  
150 partial radiative perturbation experiments, conducting two radiative transfer simulations, one  
151 without perturbation (control run) and the other with a perturbation of one atmospheric variable;  
152 the difference between these two simulations is used to calculate radiative kernel value. In both  
153 experiments, the upward, downward and net radiative fluxes at the TOA and surface are saved at  
154 each time instance and location. Then  $\Delta R_0$  can be obtained by differencing the saved radiative  
155 fluxes between the perturbed and unperturbed experiments. Dividing  $\Delta R_0$  with the perturbation  
156 of variable  $X$  ( $\Delta X_0$ ), the instantaneous radiative kernel  $K_X$  is calculated as

157

$$158 \quad K_X = \frac{\Delta R_0}{\Delta X_0} \quad (1)$$

159

160 Applying such perturbation computations to all the relevant variables (see Appendix for a  
161 detailed discussion of the procedure), we obtain instantaneous radiative kernels of these  
162 dimensionalities: the surface temperature and albedo kernels are 3-D arrays (time, latitude|73,  
163 longitude|144), and the air temperature and water vapor kernels are 4-D arrays (time, level|37,  
164 latitude|73, longitude|144).

165 To account for possible interannual variability of the radiative kernel values, we compute  
166 the kernels using atmospheric data of five calendar years: from year 2011 to 2015. Among these  
167 years, 2011 is a strong La Niña year, 2015 is a strong El Niño year. Monthly or annual mean  
168 kernels are then averaged from the instantaneous computations. For example, the LW annual

169 mean kernel of 2011 is obtained as  $K = \frac{1}{365*4} \sum_{i=1}^{365*4} K_i$  (365 is the number of days of a year and  
170 4 is because 6-hourly data are used for LW calculations) and the SW kernels,  $K =$

171  $\frac{1}{365*8} \sum_{i=1}^{365*8} K_i$  (8 is because 3-hourly data are used for SW calculations), where the index  $i$   
172 represents the time slices included in the averaging. The analyses in this work are based on  
173 multi-year mean kernels if not otherwise stated.

174

## 175 **3. Characterization of ERA5 kernels**

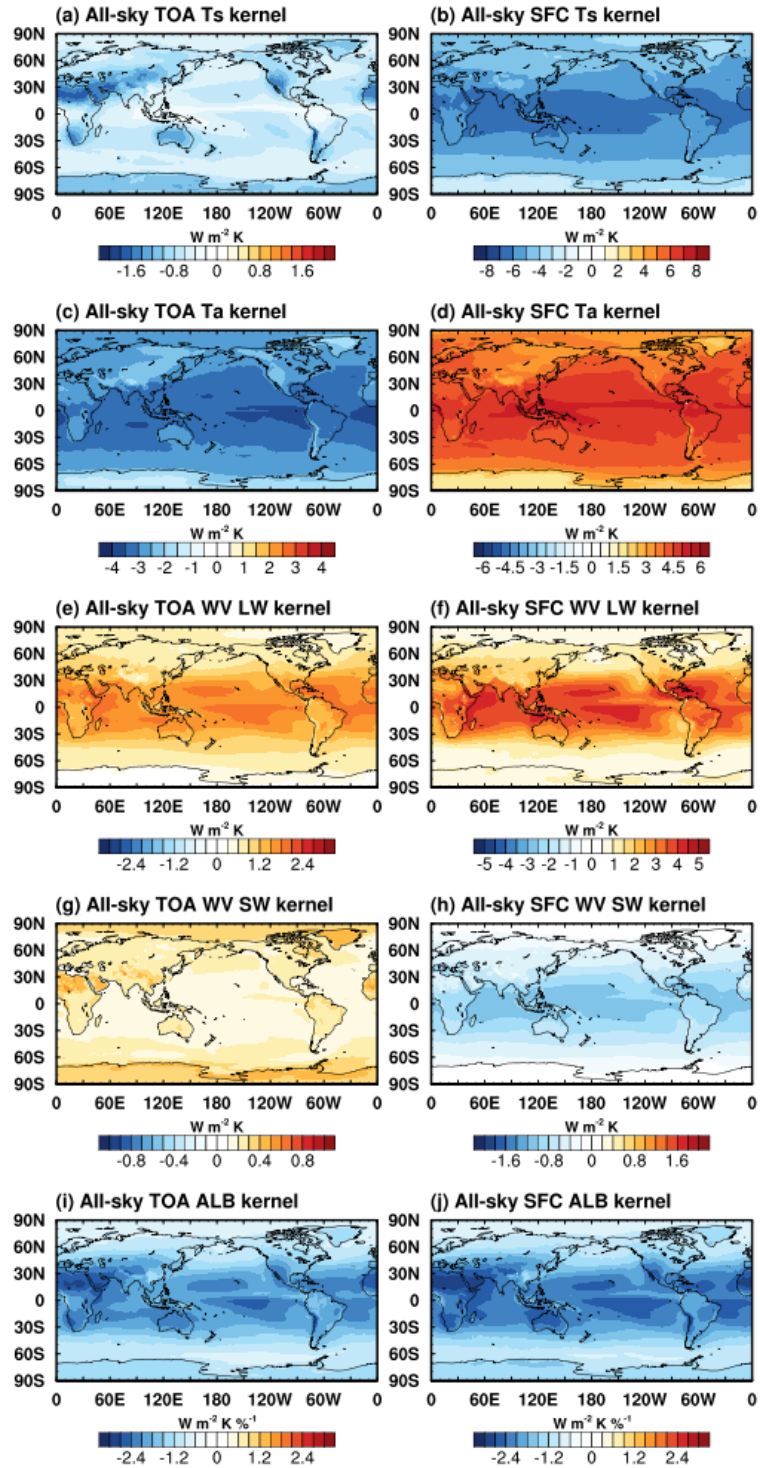
176

177

178  
179  
180  
181  
182  
183  
184  
185  
186

In this section, we first present the all-sky TOA and surface radiative sensitivity kernels quantified from the ERA5 in Figure 1 to 4 (the clear-sky kernels as well as the atmospheric kernels are shown in Figure S1-S4 for interested readers). Then, we compare ERA5 kernels with the other kernel datasets and we examine the interannual variability of the ERA5 kernel values, due to the dependency of radiative sensitivity on the background atmospheric state.

### **3.1 Distribution of radiative sensitivity**



187  
 188  
 189  
 190  
 191  
 192  
 193

Figure 1. All-sky (left) TOA and (right) surface ERA5 kernels of (a, b) surface temperature ( $T_s$ ), (c, d) air temperature ( $T_a$ ), (e, f) water vapor longwave ( $WV\ LW$ ), (g, h) water vapor shortwave ( $WV\ SW$ ) and (i, j) surface albedo ( $ALB$ ). Note that for  $T_a$ ,  $WV\ LW$ , and  $WV\ SW$  kernels, vertically integrated values are shown, which represents the sensitivity of radiative flux to a whole-column atmospheric perturbation.

194 Figure 1 summarizes the spatial distribution of all-sky ERA5 kernels for TOA and surface  
195 and Figure 2 illustrates the vertical cross-sections of zonal mean air temperature, water vapor  
196 LW and water vapor SW kernels in all-sky (see Figure S1 and S2 for results in clear-sky). For  
197 surface temperature kernel, an increase of surface temperature leads to more upwelling longwave  
198 radiation (i.e., OLR) both at the surface and TOA, therefore the kernel is negative. The TOA flux  
199 sensitivity in clear-sky (Figure S1a) is stronger than that in all-sky (Figure 1a) due to the absence  
200 of cloud, and the value increases with latitude, due to the decreasing concentration of water  
201 vapor from the tropics to the poles. The all-sky TOA sensitivity is strongly influenced by clouds,  
202 showing, for example, the fingerprint of the ITCZ in the tropical oceans (Figure 1a). The  
203 locations with less atmospheric absorption due to less water vapor or cloud, e.g., in the Tibetan  
204 Plateau and Sahara Desert regions, show relatively stronger sensitivity (Figure 1a). For the  
205 surface flux kernels, the increase of surface temperature enhances the upward emission  
206 according to the Planck function and thus the distribution follows that of surface temperature in  
207 both clear-sky and all-sky (Figure 1b).

208 For air temperature kernel, the increase of air temperature increases the OLR at TOA and  
209 also the downwelling flux at surface, so the TOA and surface kernels take negative and positive  
210 signs, respectively. The TOA kernel has maximum values in the tropics, due to the higher air  
211 temperature (Planck function) and more abundant cloud and water vapor (higher emissivity)  
212 there, and generally decreases in magnitude with latitude (Figure 1c). Unlike the TOA flux  
213 kernel, which shows comparable sensitivity to air temperature at nearly all vertical levels, the  
214 surface flux is mainly sensitive to the bottom layers (Figure 2b).

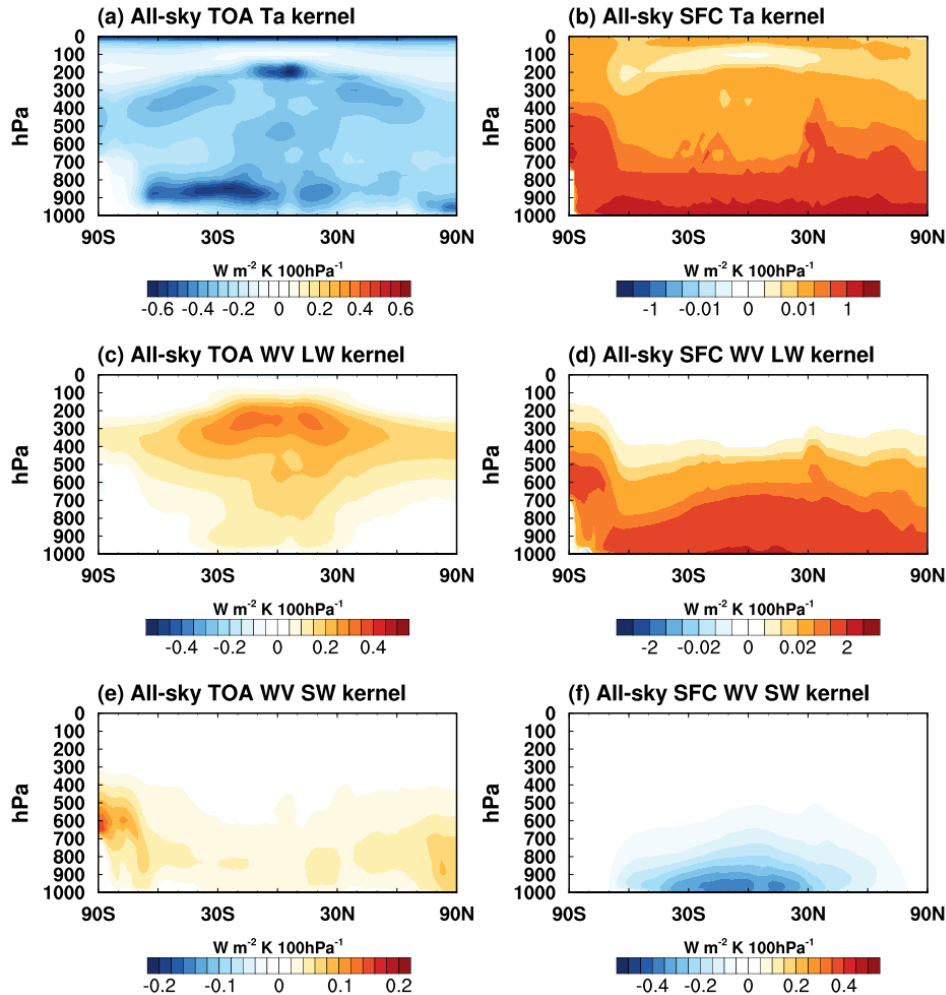
215 For water vapor LW kernel, an increase of water vapor reduces OLR at TOA and increases  
216 downwelling radiation at surface, so that the TOA and surface kernels are both positive in sign.  
217 The vertically integrated kernel values (Figure 1e and f) generally follow the temperature  
218 distribution, for example, decreasing in magnitude with latitude. In both cases, the kernel  
219 magnitude is dampened by clouds in all-sky. The vertically resolved kernels show maximum  
220 sensitivity of TOA flux to the upper troposphere (Figure 2c) and maximum sensitivity of surface  
221 flux to the bottom layers (Figure 2d), respectively. In terms of the atmospheric radiation (the  
222 convergence of the TOA and surface radiation fluxes in the atmosphere), the increase in water  
223 vapor concentration absorbs more LW in the upper troposphere than what it emits but the  
224 opposite is true in the lower troposphere (Figure S4c). Such features were discussed in previous  
225 works (e.g., Huang et al. 2007).

226 For water vapor SW kernel, an increase of water vapor absorbs solar radiation and thus  
227 reduces both the upwelling (reflected) SW flux at TOA and the downwelling SW flux at surface.  
228 As a result, the two kernels take positive and negative signs, respectively. Note the magnitude of  
229 the SW kernels is much weaker than that of the LW kernels, because water vapor absorbs the  
230 LW flux more significantly than the SW flux. One noticeable feature of the TOA kernel in clear-  
231 sky (Figure S1g) is that the magnitude over the land is stronger than that over the ocean, because  
232 the relatively higher albedo over the land reflects more SW radiation and thus enhances the  
233 absorption by the water vapor in the atmosphere. For this reason, over reflective surfaces such as  
234 the Sahara Desert and Tibetan Plateau, as well as the Poles, the sensitivity is maximized. Unlike  
235 the TOA kernel, the distribution of surface kernel follows the distribution of background water  
236 vapor concentration, with noticeable dampening by clouds (Figure 1h and 2f).

237 For surface albedo kernel, an increase of surface albedo leads to more upwelling  
238 (reflected) SW flux both at surface and TOA; therefore, the kernel is of negative sign. In clear-  
239 sky, the sensitivity strength follows the pattern of solar insolation, with some local maxima, e.g.,



240 in the Sahara Desert and Tibetan Plateau (Figure S1i and j) due to the relatively lower water  
 241 vapor concentration. In all-sky, the distribution is again influenced by cloud patterns; for  
 242 example, in the ITCZ region, the strength is much reduced as clouds reduce the solar radiation  
 243 reaching the surface and thus the sensitivity to surface albedo change (Figure 1i and j).  
 244



245  
 246 Figure 2. All-sky (left) TOA and (right) surface ERA5 vertically resolved and zonally  
 247 averaged kernels of (a, b) air temperature ( $T_a$ ), (c, d) water vapor longwave ( $WV LW$ ) and (e, f)  
 248 water vapor shortwave ( $WV SW$ ), units:  $W m^{-2} K^{-1} 100hPa^{-1}$ . Note nonlinear colorbars used for  
 249 surface air temperature and water vapor LW kernels.

250  
 251

### 252 3.2 Comparison of ERA5 kernels with other datasets

253

254 To examine the discrepancies between different kernel datasets, we select six previously  
 255 published ones for comparison. Table 1 summarizes their resolutions and the atmospheric  
 256 datasets based on which they are computed, including the GCMs: GFDL (Soden et al., 2008),  
 257 CAM3 (Shell et al., 2008), CAM5 (Pendergrass et al., 2018), and HadGEM3 (Smith et al., 2020),  
 258 a global reanalysis: ERAi (Huang et al., 2017), and satellite observations: CloudSat/CALIPSO  
 259 (Kramer et al., 2019b). This list is meant to be representative instead of exhaustive.

260  
261  
262

Table 1. Summary of radiative kernels compared in this work. Datasets with \* only have TOA kernels.

Radiative kernels	Horizontal resolution (lat*lon)	Vertical resolution	Reference
GFDL*	2x2.5	17 (pressure level)	Soden et al., 2008
CAM3*	2.8x2.8	17 (pressure level)	Shell et al., 2008
ERAi	2.5x2.5	24 (pressure level)	Huang et al., 2017
CAM5	0.94x1.25	30 (hybrid level) or 17 (pressure level)	Pendergrass et al., 2018
CloudSat	2x2.5	17 (pressure level)	Kramer et al., 2019b
HadGEM3	1.25x1.9	85 (hybrid level) or 19 (pressure level)	Smith et al., 2020
ERA5	2.5x2.5	37 (pressure level)	This study

263  
264

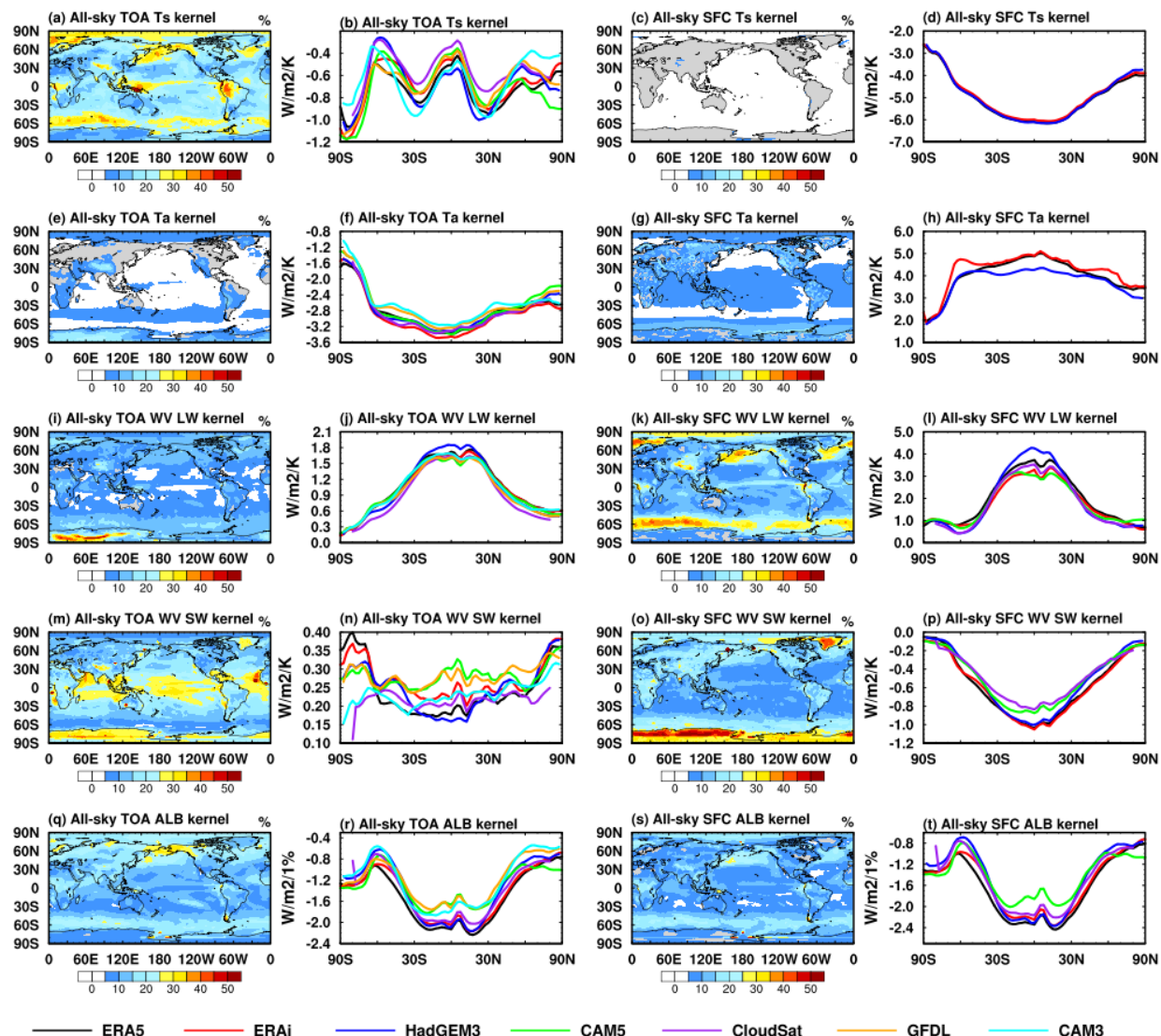
265 To facilitate an intercomparison, these kernel datasets are interpolated to the same  
266 horizontal and vertical resolutions as those of the ERA5 kernel when illustrated in Figure 3 and 4  
267 (see Figure S5 and S6 for clear-sky) and are uploaded to the same data repository of ERA5  
268 kernels. Note that the CAM5 and HadGEM3 kernels have two versions, with one defined at the  
269 raw hybrid levels and the other interpolated to pressure levels. To retain the accuracy of them as  
270 much as possible, the hybrid level version is used for the interpolation and comparison in Figures  
271 3 and 4, while in Section 4, the pressure level version is used for quantifying the feedbacks of  
272 CMIP6 models. The GFDL and CAM3 kernels are only available for TOA fluxes and are  
273 excluded for surface kernel comparisons.

274 Here we use the standard deviation (*std*) and its normalized value (*std\**) to measure the  
275 spread of the inter-kernel dataset differences:

$$276 \quad std_X = \sqrt{\frac{1}{n-1} \sum_{i=1}^n (K_X^i - \overline{K_X})^2} \quad (2)$$

$$277 \quad std_X^* = \frac{std_X}{\overline{K_X}} * 100 \quad (3)$$

278 where  $n$  is the total number of kernel datasets.  $K_X^i$  is radiative kernel of variable  $X$  from the  $i^{th}$   
279 dataset.  $\overline{K_X}$  is the multi-dataset mean of radiative kernel  $K_X$ . Note that  $\overline{K_X}$  does not represent the  
280 “truth” value, but a reference value used to measure the spread of multi-kernel values. The  
281 vertically integrated and the vertically resolved but zonally averaged distributions of fractional  
282 discrepancy (*std\**) are shown in Figures 3 and 4, respectively. The zonal mean kernel values  
283 from respective multi-datasets are shown in line plots in Figure 3 and 4. Note that some kernels  
284 exhibit abnormal values, such as the surface and air temperature kernel of the surface flux in the  
285 CAM5 and CloudSat kernels (see Appendix Figure A2), indicating inconsistent computation of  
286 their values, and thus are excluded in the corresponding  $std_X^*$  statistics in Figures 3 and 4. See  
287 more discussions in Appendix.

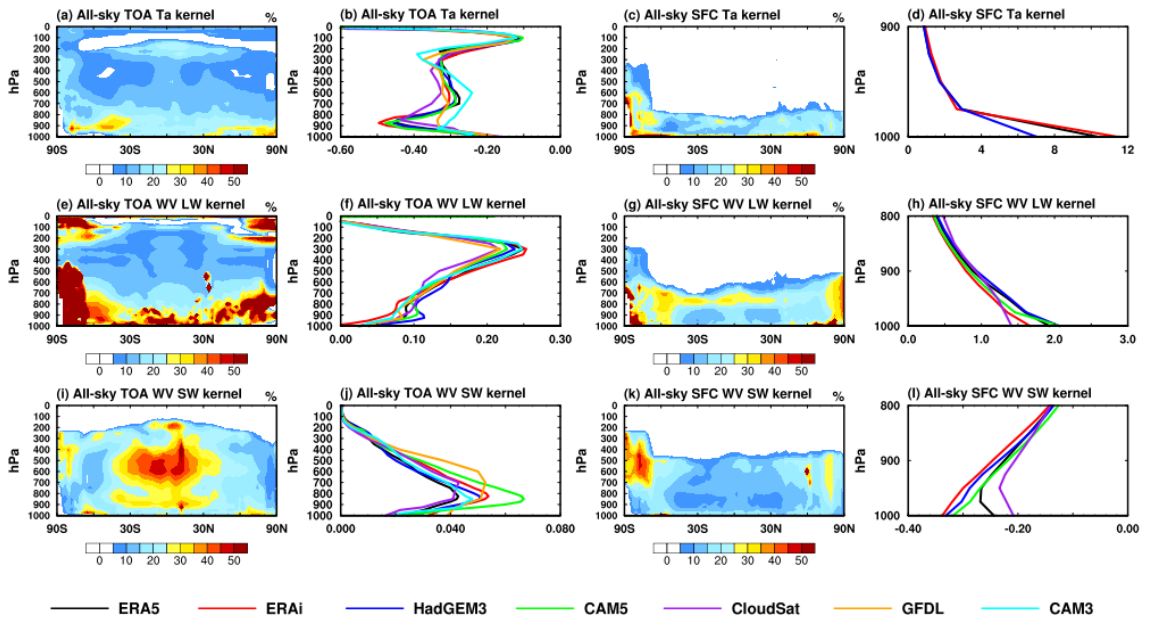


288  
 289 Figure 3. (contour plot) fraction discrepancies as measured by the normalized standard deviation  
 290 of the kernels by Eq. (3) and (line plot) zonal mean distribution of multi-kernels in all-sky.  
 291  
 292

293 The comparisons identify the following relatively larger differences in kernel values.  
 294 Among the TOA kernels, the surface temperature and albedo kernels show relatively large  
 295 discrepancies in the Arctic, Southern Ocean and over some continental regions in the tropics in  
 296 all-sky (Figure 3a and q), with the maximum discrepancy exceeding 30%; the air temperature  
 297 kernel shows larger discrepancies in the lower troposphere and tropical tropopause region  
 298 (Figure 4a); these kernel differences are likely due to the differences in cloud fields. The water  
 299 vapor LW kernel also shows noticeable fractional biases, for example, over the Antarctic region  
 300 (Figure 3i and 4e). The water vapor SW kernel shows differences in the tropical mid-troposphere  
 301 and over Antarctic in both clear-sky and all-sky (Figure 4i and S6i), leading to strong variations  
 302 in the vertical integration of sensitivity (Figure 3m and S5m), with a spread exceeding 30%. The  
 303 noticeable periodic equatorial pattern in Figure S5m is caused by the CAM3 kernel, likely due to

304 a coarser temporal resolution that does not well resolve the diurnal cycle of solar insolation in the  
 305 kernel computation.

306 For the surface kernels, the most prominent differences exist in SW radiative kernels  
 307 (Figure 3 and 4), especially in the polar regions. The discrepancy in the water vapor SW kernel  
 308 reaches 30% for vertically integrated values (Figure 3o), with noticeable biases through the  
 309 troposphere (Figure 4k). The surface albedo kernel differences are much larger in all-sky than  
 310 that in clear-sky (Figure 3 and S5), indicating that the cause is in cloud fields, and are also  
 311 noticeable in the Arctic region due to sea ice variations (Figure 3s). In the LW, the water vapor  
 312 kernels exhibit noticeable differences in the Central Pacific, Southern Ocean and Arctic in all-  
 313 sky (Figure 3k), where again the difference in cloud field is likely the cause. The air temperature  
 314 kernels show noticeable discrepancies in the bottom layers (Figure 4d), which may be caused by  
 315 inconsistency in the kernel computation and vertical resolutions (see the discussions in  
 316 Appendix).  
 317



318  
 319 Figure 4. (contour plot) Cross-section of fraction discrepancies of the radiative kernels, (line  
 320 plot) global mean vertically resolved kernels from multi-datasets in all-sky.  
 321

322 In summary, the differences among radiative kernel datasets are generally smaller in clear-  
 323 sky than in all-sky and in most cases, are mostly within 10%. However, there are some notable  
 324 regional discrepancies, for example, in the surface temperature kernel in the tropics (Figure 3a),  
 325 in the surface albedo kernel in the Arctic (Figure 3q), and in the water vapor SW kernel in the  
 326 Antarctic region (Figure 3m). As different kernel datasets are calculated using different data  
 327 sources, the discrepancies detected here are likely due to the state-dependency in the kernels,  
 328 which differ between the kernel datasets. To ascertain the state-dependency-caused kernel  
 329 uncertainty, we next examine the ERA5 kernels computed from different years, i.e., from  
 330 different atmospheric states, to investigate how much difference in radiative sensitivity can result  
 331 from the change in atmospheric state.  
 332  
 333

### 334 3.3 Interannual variation of kernel values

335

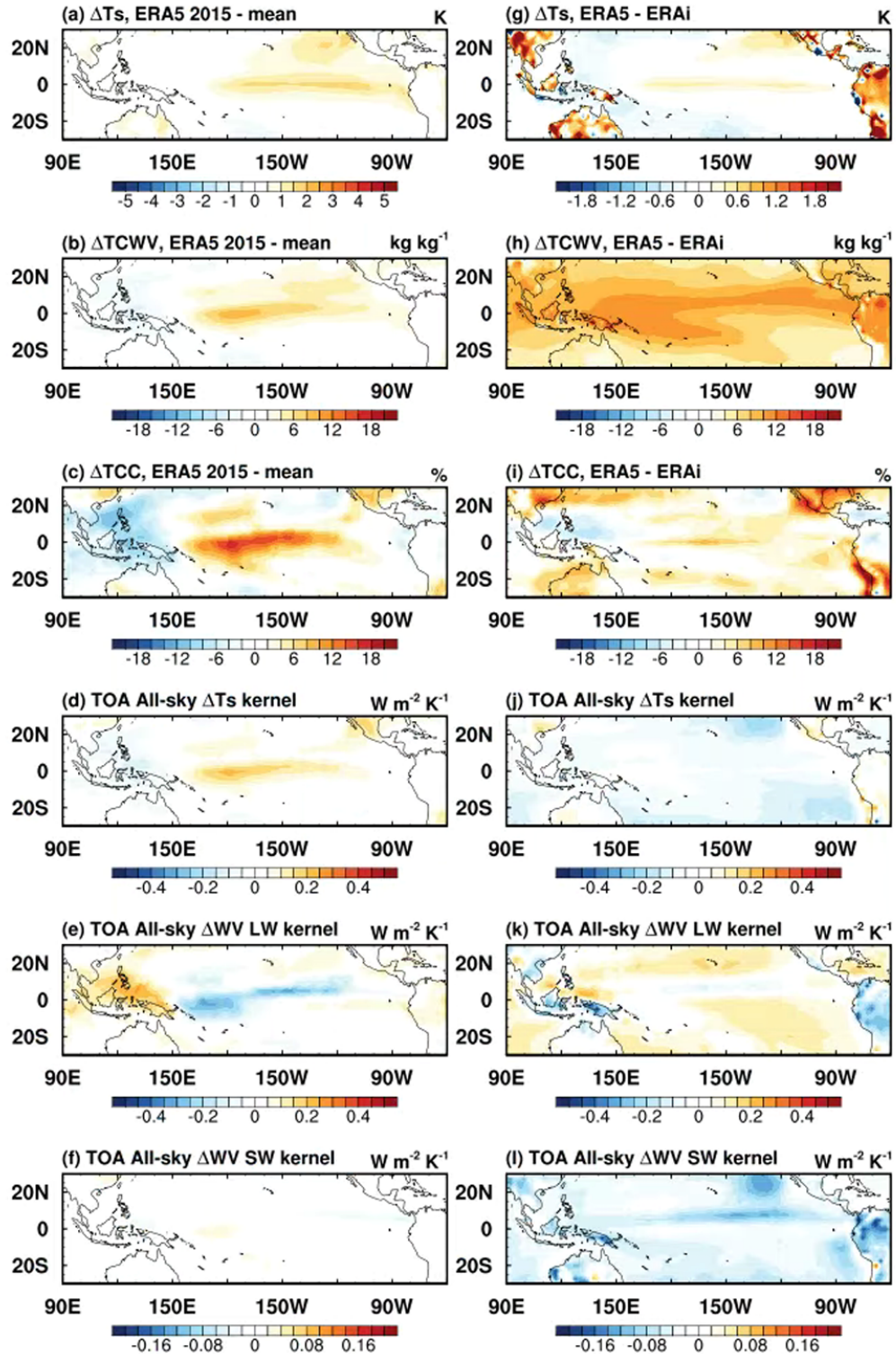
336 The intercomparison above identified several prominent inter-dataset differences in the  
337 kernel values. For example, there are noticeable differences in the values of surface temperature,  
338 albedo and water vapor kernels in the Central Pacific and Arctic region. One possible reason that  
339 may account for such differences is the atmospheric state-dependency of the kernel values.  
340 Besides the inter-model differences in the different GCM climatology, interannual variations of  
341 the atmospheric states, such as cloudiness variations in the Central Pacific region during the  
342 ENSO cycle, may affect the radiative sensitivity as some radiative kernels are calculated using  
343 one arbitrary year's data. To test this hypothesis, we use the ENSO and sea ice loss cases to  
344 demonstrate the changes in radiative sensitivity with a focus on Central Pacific and Arctic  
345 region, respectively. In the ENSO case, the variation is defined as the difference in annual mean  
346 kernel values between 2015 and 5-year mean (from 2011 to 2015), which have the annual mean  
347 sea surface temperature anomalies in the Niño 3.4 region (5N-5S, 190-240E) over +2.0K. In the  
348 sea ice loss case, the variation is calculated as the difference in September between year 2012  
349 and 2013, as the sea ice cover in 2012 was reported to be the lowest level in the satellite  
350 observation era. In addition, we further show the comparison between ERA5 and ERAi kernels  
351 (in Figure 5), which was also calculated by RRTMG and averaged from 5 years' calculations  
352 (2008-2012), to compare the inter-kernel difference and interannual difference in kernel values.

353 To save space, here we only highlight the most prominent differences. Figure 5a-c show  
354 the differences in skin temperature, total column water vapor and total cloud cover due to ENSO  
355 and Figure 5d-f summarize the corresponding differences in all-sky TOA kernels. As the skin  
356 temperature in the Central Pacific warms over 2K (Figure 5a) during ENSO, the increases in  
357 water vapor concentration and cloud fraction (Figure 5b and c) reduce the sensitivity of TOA  
358 flux to surface temperature change by about  $0.2 \text{ W m}^{-2} \text{ K}^{-1}$  (about 33%) (Figure 5d). The  
359 moistening in the Central Pacific (Figure 5b) enhances the TOA water vapor LW sensitivity in  
360 clear-sky (Figure S7b), while in all-sky the enhanced convection and associated total cloud cover  
361 in this region lead to a weakened TOA water vapor LW radiative sensitivity (Figure 5e) despite  
362 the moist anomaly, and the decrease is almost contributed from the whole troposphere (Figure  
363 S8c). The water vapor SW kernel discrepancy is less pronounced (Figure 5f).

364 Comparing the 5-year averaged all-sky ERA5 and ERAi kernels, we find that the  
365 atmospheric state differences also exist between the atmospheric datasets on which the kernels  
366 are computed from. For example, the ERA5 shows similar, but less pronounced, warming  
367 anomalies in sea surface temperature in the Central Pacific compared to ERAi, partly due to the  
368 strong El Nino year (2015) included in the ERA5 dataset. ERA5 data also shows more water  
369 vapor and cloud cover (Figure 5h and i). As a result, the surface temperature kernel computed  
370 from ERA5 shows less TOA radiative sensitivity to surface temperature than that from ERAi. It  
371 is also noticed that the ERA5 water vapor SW kernel shows lower sensitivity and mainly comes  
372 from the contributions in mid-to-low troposphere (Figure S8f), which corresponds to the  
373 discrepancy noticed in Figure 4i. The clear-sky kernels are of much less differences (Figure S7),  
374 confirming that the difference in clouds is the main cause of the all-sky kernel differences, which  
375 also correspond to the discrepancies shown in the multi-kernel comparisons in Figure 3a, i, and  
376 m.

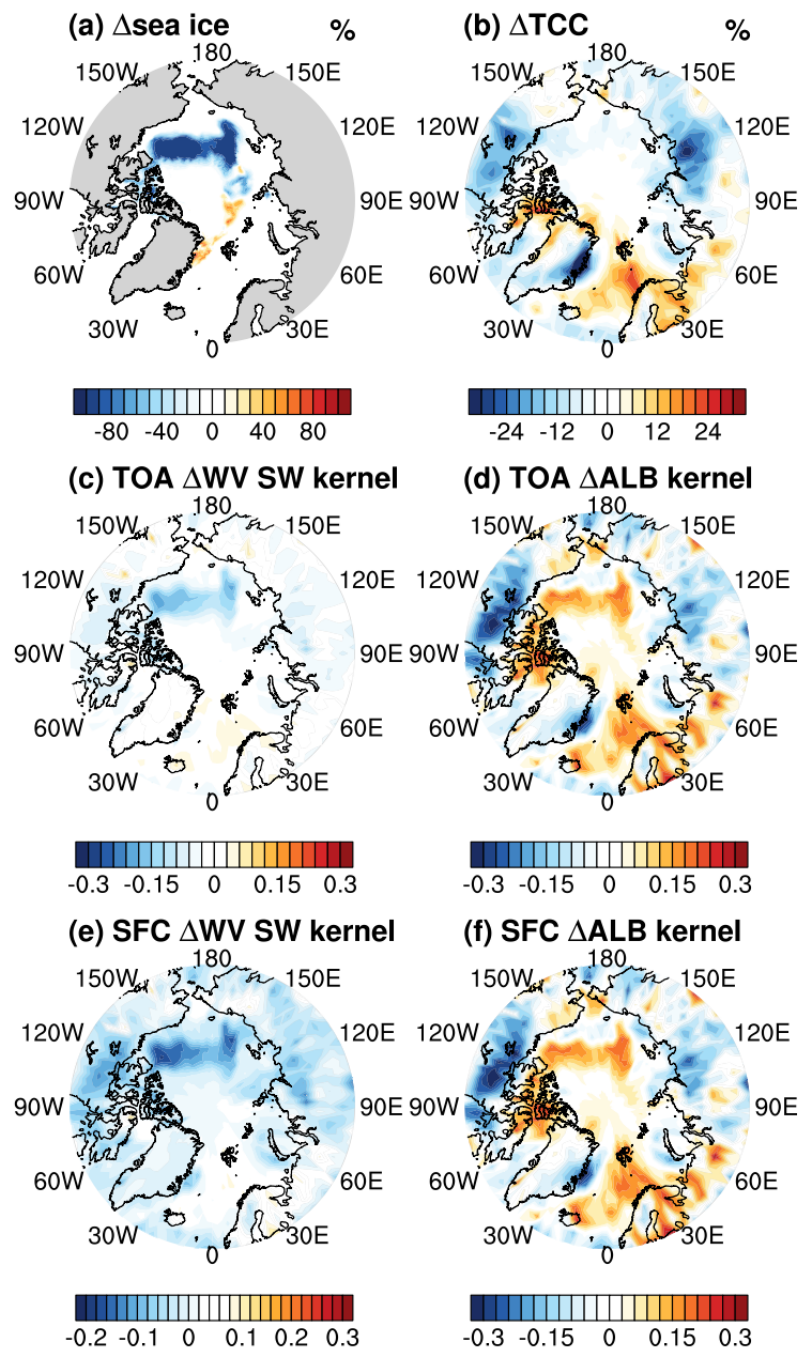
377





378  
 379  
 380  
 381  
 382  
 383

Figure 5. Differences in climate states and all-sky kernel values (left) between an arbitrary year (2015) and a 5-year mean of ERA5 and (right) between the 5-year means of ERA5 and ERAi datasets: (a, g) skin temperature, (b, h) total column water vapor (TCWV), (c, i) total cloud cover (TCC), (d, j) TOA skin temperature kernel, (e, k) TOA vertically integrated water vapor LW kernel and (f, l) TOA vertically integrated water vapor SW kernel.



385

386

387

388

389

390

391

392

393

Figure 6. September differences between 2012 and 2013 in (a) sea ice concentration, (b) total cloud cover (TCC), and the differences in (c, e) water vapor SW kernel for TOA and surface fluxes, units:  $\text{W m}^{-2} \text{K}^{-1}$ , (d, f) surface albedo kernel for TOA and surface fluxes, units:  $\text{W m}^{-2} 1\%^{-1}$ .

In the sea ice loss case, the reduction of sea ice in the Arctic region (Figure 6a) leads to a significant decrease of radiative sensitivity to surface albedo (Figure 6d and f), with the maximum difference exceeding 30%. The cloud cover change also contributes to changes in

394 surface albedo kernel values due to the coupling effect between cloud and surface albedo (e.g.,  
 395 see Huang et al., 2021b), which for example is seen in the Siberia and to the west coastline of  
 396 Europe. The change in sea ice also leads to a significant decrease in the TOA sensitivity and an  
 397 increase of surface sensitivity to water vapor, respectively (Figure 6c and e), with the maximum  
 398 changes exceeding 80% for surface. All these results confirm the state-dependency of radiative  
 399 kernels (e.g., Riihelä et al., 2021).

400 In summary, these quantitatively large interannual differences, as well as their locations,  
 401 affirm that some discrepancies between the radiative kernels are caused by the difference in  
 402 atmospheric states and partly explain the inter-dataset kernel differences seen in Figure 3 and 4.  
 403 Nevertheless, it ought to be noted that the differences are localized and because of that do not  
 404 cause significant biases in the global mean feedback values (see Section 4). The results above  
 405 also show that kernel values based on one arbitrary year may be regionally biased. If only one  
 406 year's atmospheric profiles are used to generate radiative kernels, we recommend selecting a year  
 407 without significant anomalies in atmospheric states, e.g., due to El Nino or severe sea ice loss.  
 408

409

#### 410 **4. Feedback quantification**

411

412 In this section, we apply different kernels to quantifying the radiative feedbacks in one  
 413 quadrupling CO<sub>2</sub> experiment (abrupt4xCO<sub>2</sub>) of CMIP6 models. This experiment is selected  
 414 because it has been used by a number of studies for forcing and feedback analyses (e.g., Zelinka  
 415 et al., 2020), which we can compare our results to. The CMIP6 models used in this assessment  
 416 are listed in Table 2. Note that the standard outputs at 19 pressure levels from the models and  
 417 correspondingly the kernel values, including CAM5 and HadGEM3, provided at the pressure  
 418 levels are used in this section.  
 419

419

420

Table 2. Summary of CMIP6 models used in this study.

Models	Horizontal resolution (lat*lon)	Vertical levels	Reference
CESM2	0.9*1.25	32 levels to 2.26 hPa	Danabasoglu et al. (2020)
CNRM-CM6-1	1.4*1.4	91 levels to 0.01hPa	Voltaire et al. (2019)
EC-Earth3	0.7*0.7	91 levels to 90 km	Döscher et al. (2022)
HadGEM3-GC31-LL	1.25*1.875	85 levels to 85km	Williams et al. (2018)
IPSL-CM6A-LR	1.3*2.5	79 levels to 80km	Boucher et al. (2020)
MPI-ESM1-2-LR	1.875*1.875	47 levels to 0.01hPa	Mauritsen et al. (2019)

421

422

#### 423 **4.1 Analysis procedure**

424

425 To quantify the radiative feedbacks, data from two experiments as documented by Eyring  
 426 et al. (2016) and Pincus et al. (2016) are used: abrupt4xCO<sub>2</sub>, simulations with an instantaneous  
 427 quadrupling of CO<sub>2</sub> concentration of year 1850, piClim-4xCO<sub>2</sub>, simulations with SST and sea ice  
 428 concentrations fixed at the climatology of pre-industrial control experiment and CO<sub>2</sub>  
 429 concentration quadrupled. In each experiment, a 20-year period at the end of the simulation in



430 each model is used. For example, in the models where the abrupt4xCO<sub>2</sub> simulation is longer than  
 431 150 years, the simulations from the last 20 years rather than those from years 131 to 150 are used  
 432 for the calculation. Following the previous studies (e.g., Smith et al., 2020; Zelinka et al., 2020),  
 433 radiative feedbacks are diagnosed using the difference of atmospheric variables between the  
 434 abrupt4xCO<sub>2</sub> and piClim-4xCO<sub>2</sub> experiments. It is worth noting that the method used in this  
 435 study is slightly different from that in Zelinka et al. (2020), in which piControl simulation was  
 436 used as the climatology baseline and the feedbacks were integrated from the surface to the  
 437 tropopause (as opposed to model top) to remove the rapid adjustment, although the quantitative  
 438 differences in the global mean feedback values are small.

439 To detail the analysis procedure, firstly, all variables including radiative fluxes and  
 440 atmospheric variables from CMIP6 models are interpolated to the horizontal and vertical  
 441 resolution of the kernel itself. Note that for CAM3, GFDL, CloudSat and CAM5 kernels, they  
 442 only have 17 pressure levels which are two layers (1hPa and 5hPa) fewer than the CMIP6  
 443 standard model output. To address this issue, the contribution of the two missing layers is  
 444 calculated using other kernels (e.g., ERA5) and found to have negligible effect on the global  
 445 mean feedback value. Hence, when using these three kernels, the contributions from 10hPa  
 446 above are ignored.

447 Secondly, the non-cloud radiative feedback of atmospheric variable  $X$  ( $\Delta R_X$ ) is calculated  
 448 as:

$$449 \quad \Delta R_X = K_X \cdot \Delta X \quad (4)$$

450 with units in  $W m^{-2}$ , where  $K_X$  is the radiative kernel of variable  $X$  and  $\Delta X$  is the anomaly of  $X$   
 451 measured by the difference between abrupt4xCO<sub>2</sub> and piClim-4xCO<sub>2</sub>, and represents the  
 452 anomalies of surface temperature ( $\Delta T_s$ ), air temperature ( $\Delta T_a$ ), water vapor ( $\Delta WV$ ) and surface  
 453 albedo ( $\Delta ALB$ ). For the 2D radiative kernels (surface temperature and surface albedo),  $K_X$  and  
 454  $\Delta X$  have just single layer values and  $\Delta R_X$  is simply the product of these two terms. For the 3D  
 455 radiative kernels (air temperature and water vapor), both  $K_X$  and  $\Delta X$  are vectors of pressure  
 456 levels and  $\Delta R_X$  is the dot product of  $K_X$  and  $\Delta X$  and is integrated from the TOA to 1000hPa.  
 457 Note that if  $K_X$  is normalized with unit pressure thickness (e.g.,  $W m^{-2} K^{-1} 100hPa^{-1}$ ), the layer  
 458 thickness must be taken into account when calculating  $dR_X$ . See Appendix for further discussion  
 459 on the application of thickness-weighted kernels.

460 Finally, cloud feedbacks are diagnosed using the adjusted cloud-radiative forcing method  
 461 (Shell et al., 2008). Here we compute the residual term in clear-sky as:

$$462 \quad res^o = \sum \Delta R_X^o - \Delta R^o \quad (5)$$

463 which represents the unexplained part of radiation budget change, and assuming the all-sky  
 464 decomposition has the same non-closure residual, the cloud feedback is measured as

$$465 \quad \Delta R_C = \Delta R - \sum \Delta R_X + res^o \quad (6)$$

466 where the superscript  $o$  represents clear-sky quantities.  $\sum \Delta R_X^o$  and  $\sum \Delta R_X$  are the sum of non-  
 467 cloud feedbacks in clear-sky and all-sky, respectively, diagnosed by multiplying the radiative  
 468 kernel with the atmospheric responses measured as the difference between abrupt4xCO<sub>2</sub> and  
 469 piClim-4xCO<sub>2</sub> experiments.  $\Delta R^o$  and  $\Delta R$  are the total radiation change in clear-sky and all-sky,  
 470 respectively, calculated as the difference in the GCM-simulated radiative fluxes between two  
 471 experiments.

472 The feedback parameters,  $\lambda_X$ , in the units of  $W m^{-2} K^{-1}$ , are then obtained by normalizing  
 473 the feedback flux changes  $\Delta R_X$  by the global mean surface temperature change  $\Delta T_s$  in the  
 474 abrupt4xCO<sub>2</sub> experiment:

$$475 \quad \lambda_X = \Delta R_X / \Delta T_s \quad (7)$$

476  
477  
478  
479

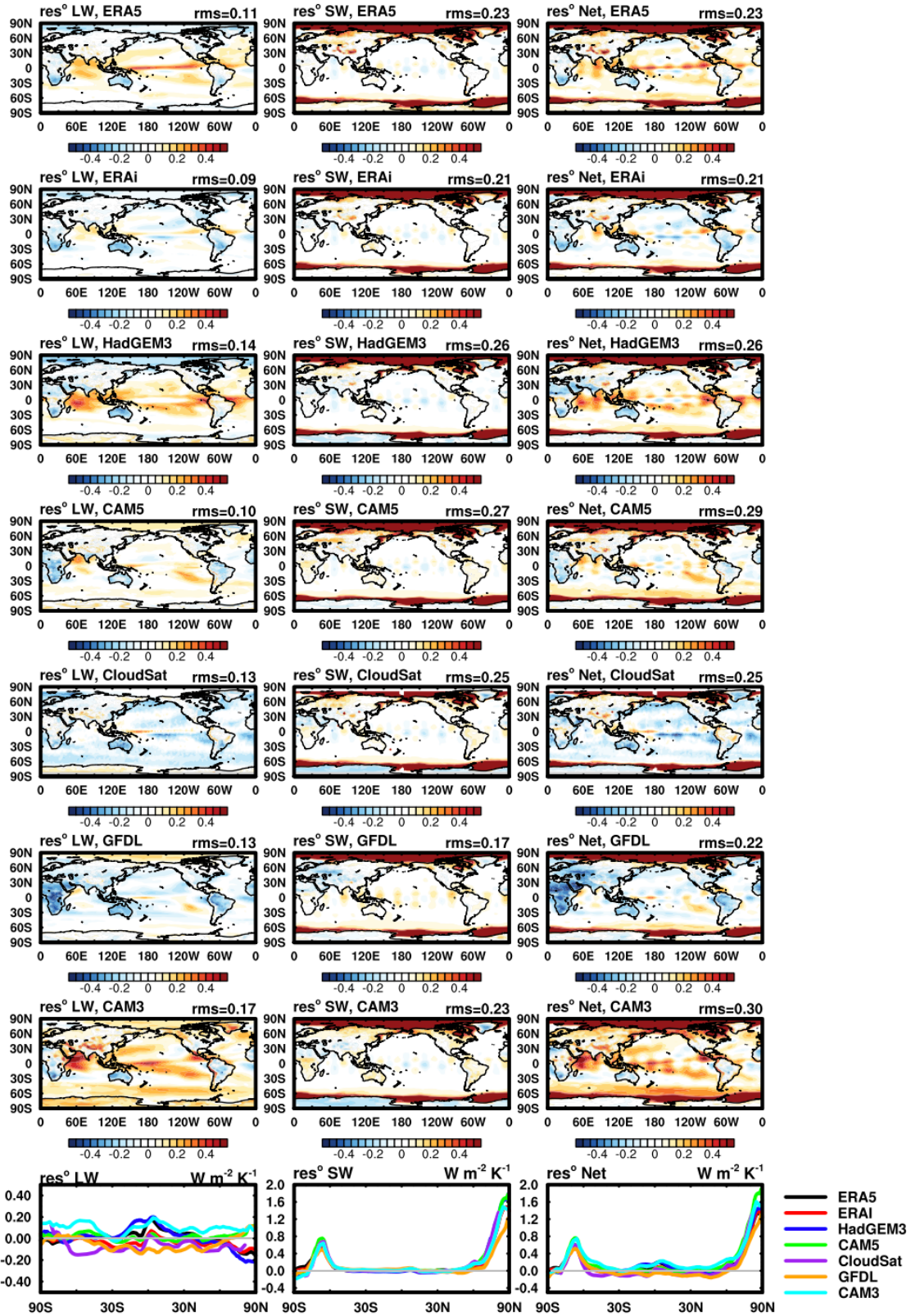
## 4.2 TOA feedbacks

480 The residual term ( $res^o$ ) measures the unexplained radiation change in the feedback  
481 analysis and provides a useful overall indication of the soundness of the feedback quantification.  
482 Figure 7 illustrates the residual term for the TOA flux decomposition when different kernels are  
483 used to diagnose the multi-model mean feedbacks. In terms of the global mean, all residual terms  
484 are of small magnitude, no matter which kernel dataset is used (Figure 8 and Table S1).  
485 However, there are some noticeable local residuals, especially for the SW budget, e.g., in the  
486 Arctic region and around the Antarctic continent where sea ice changes the most (mid-column in  
487 Figure 7). While the non-zero magnitude of the residual is partly due to nonlinearity in the  
488 radiation decomposition, e.g., possible coupling between surface albedo and water vapor (Huang  
489 et al., 2021b), the spread among the kernel results as evidenced by the line plots of Figure 7 is  
490 attributable to the discrepancies in the SW radiative kernels as revealed by the comparisons in  
491 Section 3. In the LW, the residual is generally small compared with the total feedback. In  
492 summary, the residual terms for the TOA budget are small in terms of the global mean feedback  
493 strengths, affirming the validity of the radiative kernels for feedback quantification. Here, we use  
494 the spatial root-mean square (RMS) of the residuals to quantify the regional biases, which are  
495 shown by the numbers on the right corner of each panel in Figure 7. For LW, results from ERA5,  
496 ERAi and CAM5 kernels show relatively smaller regional biases compared to those from  
497 HadGM3, CloudSat and CAM3 kernels. For SW, all kernel datasets have similar regional non-  
498 closures, for example, in the Polar regions (Figure 7 and 8). This is largely caused by the non-  
499 linearity in albedo feedback and also the coupling effect between water vapor and surface albedo  
500 feedbacks (Huang et al., 2021b; Block and Mauritsen, 2013). In summary, these results suggest  
501 that for the TOA feedback quantification, the performance of ERA5 kernel is comparable to the  
502 other datasets.

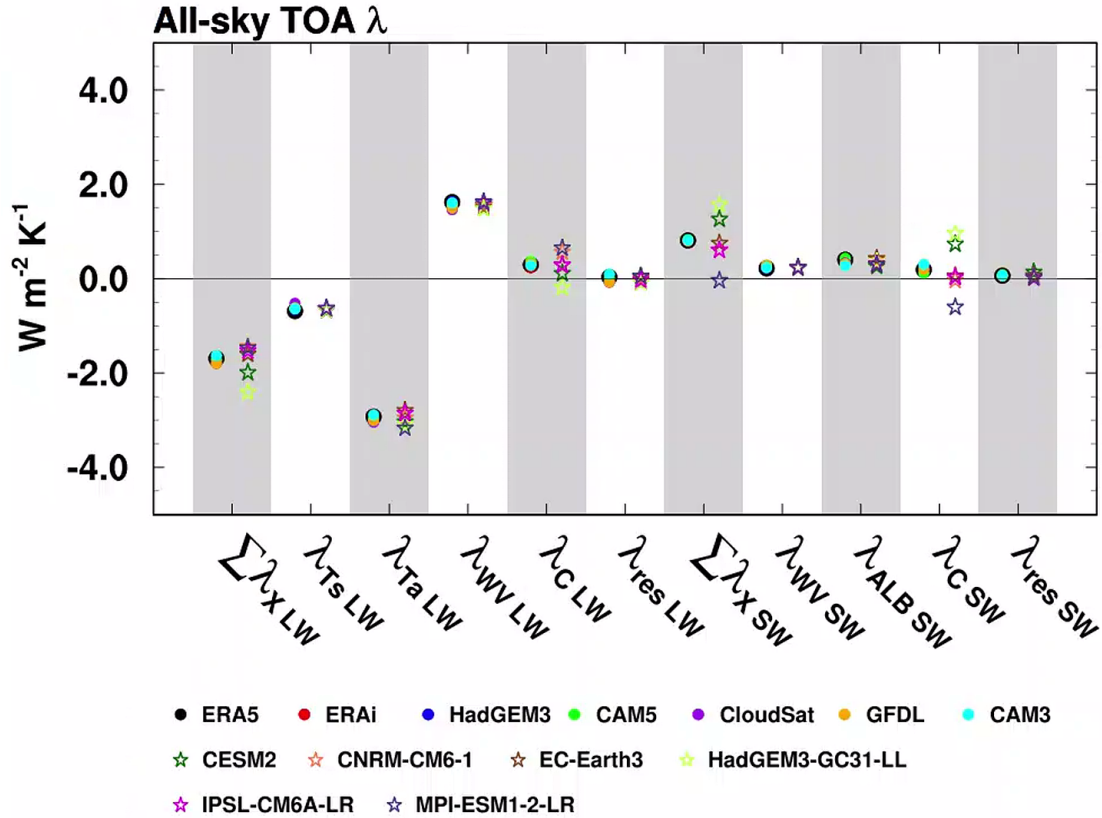
503 Figure 8 compares the spreads of feedback values resulted from the differences in kernels  
504 and those from the different projections of GCMs. In general, feedbacks from different kernel  
505 datasets overlap each other, even for cloud feedbacks, affirming a good consistency between the  
506 results computed from different kernel datasets. However, the spread across the GCMs is  
507 considerably larger, suggesting the overall feedback uncertainty is dominated by inter-model  
508 spread rather than the kernel uncertainty. The values of the feedbacks from each model and  
509 kernel datasets are shown in Table S1 and S2 for readers who are interested. These results are  
510 consistent with other published results. For example, compared with the results of Zelinka et al.  
511 (2020) based on the ERAi kernel, the kernel-diagnosed overall feedback parameter in the two  
512 results is  $-0.87 \text{ W m}^{-2} \text{ K}^{-1}$  and  $-0.85 \text{ W m}^{-2} \text{ K}^{-1}$  for the CNRM-CM6-1 model and  $-0.81 \text{ W m}^{-2} \text{ K}^{-1}$   
513 and  $-0.84 \text{ W m}^{-2} \text{ K}^{-1}$  for the HadGEM3-GC3-LL model.

514 In summary, in terms of TOA feedback values, the inter-kernel differences lead to small  
515 uncertainty in the analyzed non-cloud feedbacks; the kernel-induced uncertainty in cloud  
516 feedback is relatively larger (Table S2), with the inter-kernel spread in cloud LW feedback  
517 almost equally from the spread in surface and air temperature feedback and water vapor LW  
518 feedback, and the inter-kernel spread in cloud SW feedback more from the spread in surface  
519 albedo feedback than from water vapor SW feedback (not shown); despite this, this uncertainty  
520 is considerably less than the inter-GCM cloud feedback spread.

521



524 Figure 7. The residuals ( $res^o$ ) in the multi-model mean TOA feedback decomposition  
 525 when different kernels are used, (left column) LW, (mid-column) SW, (right-column) Net, the  
 526 sum of LW and SW. The three line-plots in the bottom row are the zonal mean residuals.  
 527 Numbers on the right corner in each panel are the spatial root-mean-square values.  
 528



529 Figure 8. Global mean TOA feedback parameters in all-sky diagnosed by the kernels list in Table  
 530 1 across CMIP6 models. Dot marks represent multi-model mean values computed from different  
 531 kernel datasets. Pentagrams represent the multi-kernel mean results computed from different  
 532 GCMs.  
 533

### 534 4.3 Surface feedbacks

535  
 536 Next, we examine how the inter-kernel differences lead to uncertainty in the analyzed  
 537 surface feedbacks.

538 Figure 9 shows the residual distribution. We find that when the ERA5 and ERAi kernels  
 539 are used for the feedback analysis, the non-closure residual in the surface budget is comparable  
 540 in magnitude to the TOA analysis. This suggests that the surface kernels afford a valid tool for  
 541 the surface feedback analysis. However, some prominent biases are noticed for other kernel  
 542 datasets. For example, the HadGEM3 kernels, show especially an underestimation in air  
 543 temperature feedback, likely due to a biased sensitivity of the bottom atmospheric layer (see  
 544 Appendix for more discussions). The sum of global mean surface and air temperature feedback  
 545 parameter measured by the HadGEM3 kernel is around  $-3.70 \text{ W m}^{-2} \text{ K}^{-1}$  (Table S4, compared to  
 546  
 547

548 around  $-1.0 \text{ W m}^{-2} \text{ K}^{-1}$  measured by the other kernels), and the non-closure residual is as large as  
549  $-3.0 \text{ W m}^{-2} \text{ K}^{-1}$  (Table S2, compared to  $0.1 \text{ W m}^{-2} \text{ K}^{-1}$  in the others). For this reason, the result  
550 from HadGEM3 kernel is excluded for the multi-kernel statistics in Figure 10, Table S3 and S4,  
551 but listed in a separate row for comparison. From either the spatial distribution of residual term  
552 or the spatial RMS residuals, the ERA5 kernel and ERAi kernel show a superior performance  
553 than other datasets. The use of ERA5 kernels may be advantageous for diagnosing the surface  
554 radiation budget, considering that ERA5 data is a newer version reanalysis dataset from ECMWF  
555 compared with ERAi and its data quality has been widely validated.

556 Figure 10 compares the inter-model and inter-kernel spreads for the surface feedbacks.  
557 Unlike the results for TOA, the inter-kernel spread can be as large as the inter-model spread, for  
558 example, in LW surface temperature feedback, air temperature feedback and water vapor  
559 feedback. The sum of air temperature and surface temperature feedbacks shows better  
560 consistency compared with the respective components, except for HadGEM3 kernel, which is  
561 due to the reason discussed in the Appendix - possibly wrong quantification of surface  
562 temperature effect. In SW, the multi-kernel results are close to each other, showing smaller inter-  
563 kernel spreads than the inter-model spreads.

564 In summary, we find the surface feedback decomposition can achieve similar level of  
565 radiation closure to the TOA analysis when using ERA5 kernels, affirming the validity of kernels  
566 for diagnosing the surface radiative feedback. However, the results qualitatively vary depending  
567 on which kernel dataset is used, indicating errors in the computation of some kernels.

568  
569



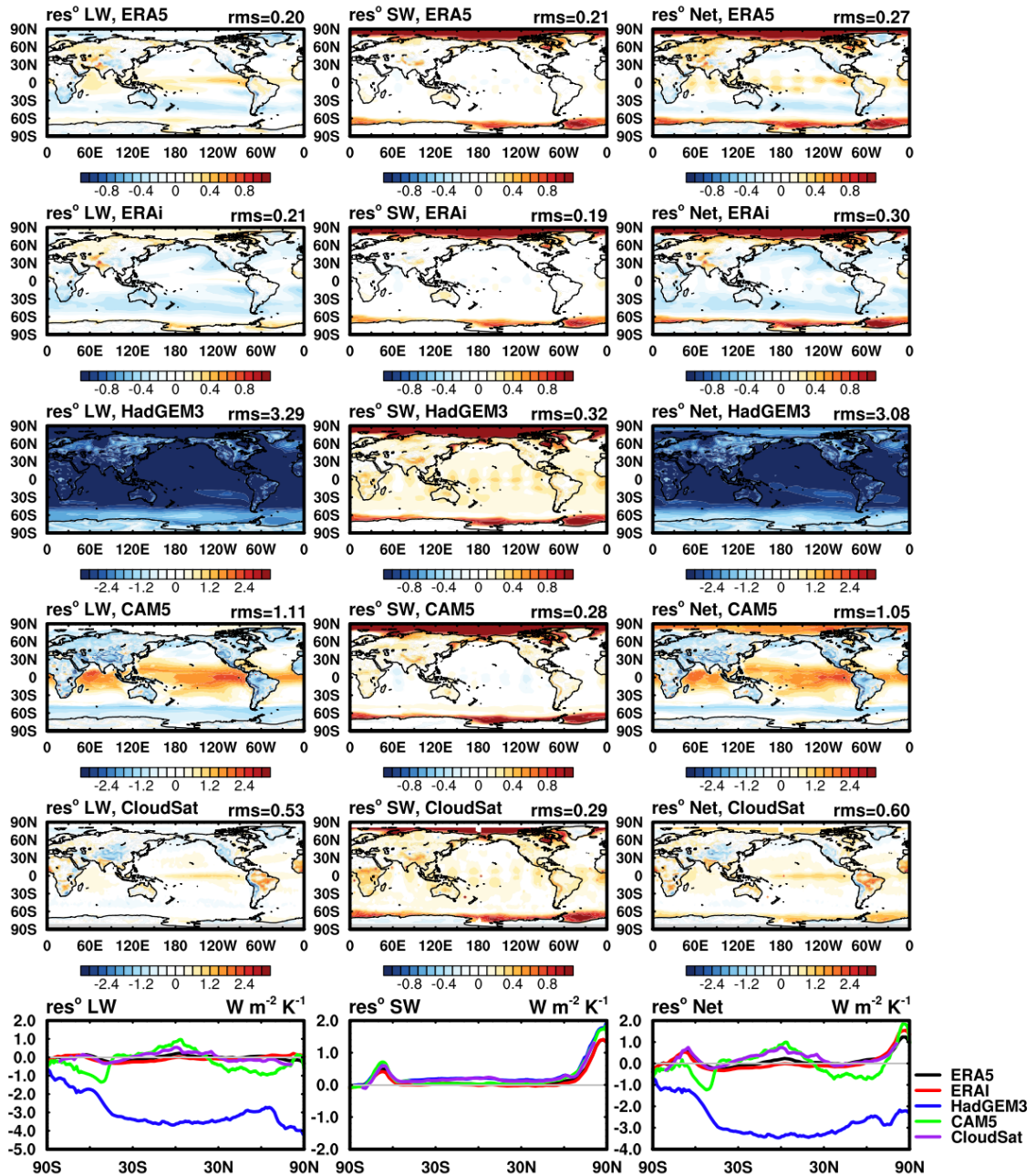
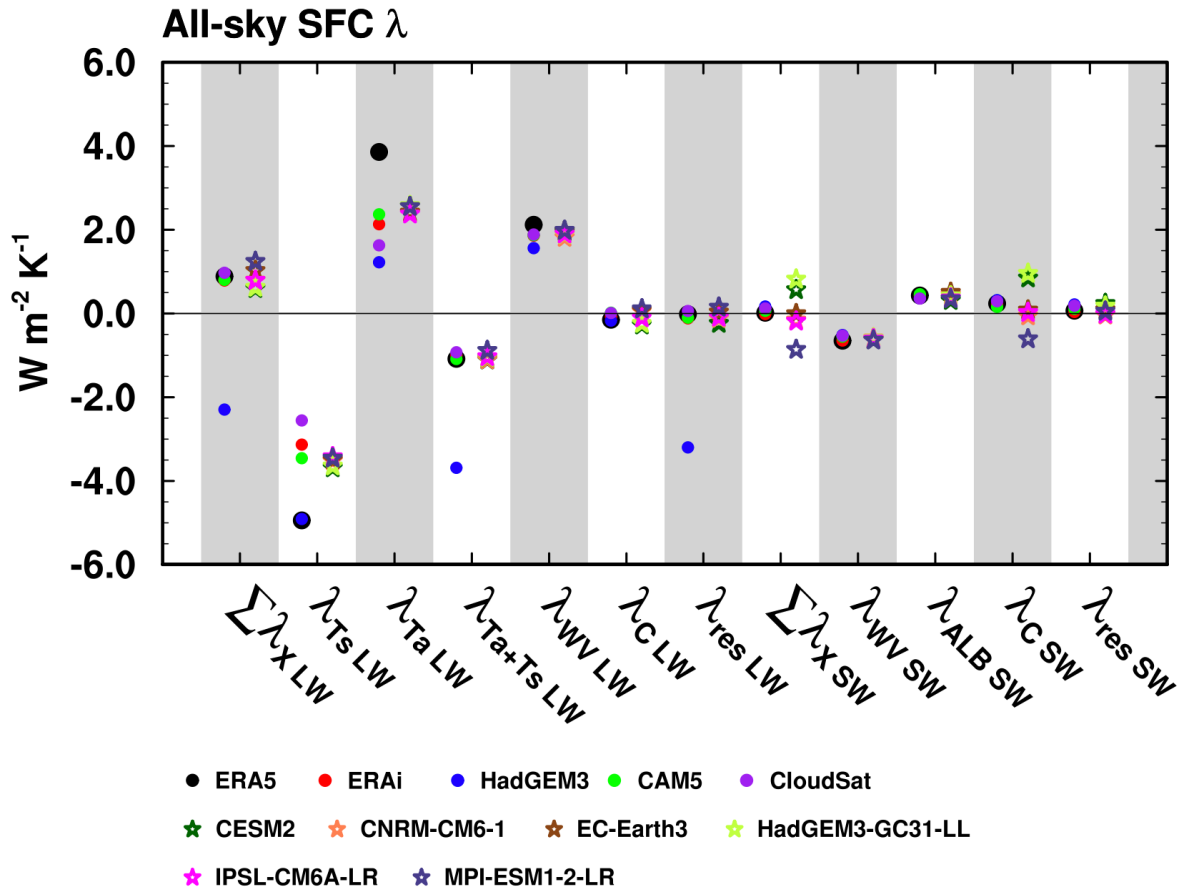


Figure 9. Similar to Figure 8, but for the surface feedback analysis.

570  
571  
572



573 Figure 10. Similar to Figure 8, but for the surface feedback parameter.  
 574  
 575

576  
 577 **5. Data availability**  
 578

579 The datasets contain the multi-year averaged monthly mean TOA and surface kernel for  
 580 surface temperature, air temperature, surface albedo and water vapor (LW and SW) and are  
 581 available at: <http://dx.doi.org/10.17632/vmg3s67568.2> (Huang and Huang, 2023).  
 582

583 **6. Conclusions and discussions**  
 584

585 In this paper, we present a newly generated set of ERA5-based radiative kernels of  
 586 surface and air temperatures, water vapor and surface albedo, for both TOA and surface radiation  
 587 fluxes. We also compare them with other published kernels, including the kernel values and the  
 588 kernel-diagnosed radiative feedbacks for both the TOA and surface radiation budgets.

589 For the TOA kernels, the results here affirm general consistency among the different  
 590 kernel datasets, and the discrepancies are generally within 10% in terms of vertically integrated  
 591 or globally averaged radiative sensitivity, although some relatively larger regional biases are  
 592 noticed, including those in the surface temperature kernel in the tropics (Figure 3a), those in the  
 593 surface albedo kernel in the Arctic (Figure 3q) and those in the water vapor shortwave kernel in

594 the Antarctica (Figure 3m), which is partly due to the dependence of radiative sensitivity on  
595 background climate states.

596 For the surface kernels, more prominent inter-kernel differences are found. For example,  
597 the differences in the water vapor shortwave kernel in the Antarctic (Figure 3o) and in the  
598 surface albedo kernel in the Arctic (Figure 3s) can reach 30%. Some kernels have considerably  
599 biased air temperature sensitivity values in the bottom atmospheric layers, which is likely due to  
600 improper treatment in the perturbation experiments used for kernel computation. The differences  
601 in both TOA and surface kernels discovered here affirm the importance of validating the  
602 radiative sensitivity as noted by Huang and Wang (2019) and Pincus et al. (2020).

603 The investigation of interannual variability in ERA5 kernels affirm the dependence of  
604 radiative sensitivity on atmospheric state and the further comparison between ERAi and ERA5  
605 kernel (Figure 5) reveals the effects of clouds on the kernel values, which explains the  
606 discrepancies of multi-kernel datasets (Figure 3).

607 Applying the different kernels to quantifying the TOA and surface radiative feedbacks,  
608 we find that for TOA feedback quantification, the ERA5 kernels are as accurate as other kernel  
609 datasets, while for surface feedback, ERA5 and ERAi kernels show superior accuracy compared  
610 with other datasets. Considering the strengths of the ERA5 dataset in representing the  
611 atmospheric states, we recommend the use of ERA5 kernels.

612 In addition, we compare the feedback differences caused by using different kernels and  
613 also the inter-GCM spread of the feedback values (when measured by the same kernel). We find  
614 the kernel difference is not a major cause of the inter-GCM TOA feedback spread (Figure 7 and  
615 8). This finding is consistent with the previous assessments (e.g., Soden et al., 2008; Jonko et al.,  
616 2012; Vial et al. 2013).

617 Radiation closure tests show that the unexplained residuals are generally within 10% for  
618 both TOA and surface analyses in terms of the global mean feedback, affirming the validity of  
619 the kernels for feedback quantification for both budgets. This suggests that the large non-closure  
620 residuals reported in some previous studies (e.g., Vargas Zeppetello, et al., 2019) are likely due  
621 to kernel inaccuracy rather than the limitation of the kernel method. However, there are more  
622 significant local non-closures, for example, in the shortwave in the Arctic region and around the  
623 Antarctic continent, which is contributed, but cannot be fully explained, by the kernel  
624 uncertainty. This points to the accuracy limit of the kernel (linear) method and calls for more  
625 advanced methods, such as the neural network method (Zhu et al., 2019), for local feedback  
626 analysis.

627

628

### 629 **Author contributions**

630

631 HH produced the ERA5 radiative kernel and provided calculations of the inter-kernel  
632 comparison and feedback analysis. Both HH and YH led the writing of the manuscript.

633

### 634 **Competing interests**

635 The authors declare that they have no conflict of interest.

636

### 637 **Acknowledgements**

638



639 We thank Mark Zelinka, Ryan Kramer and one anonymous reviewer for their helpful  
640 reviews. We acknowledge the grants from the Natural Sciences and Engineering Research  
641 Council of Canada (RGPIN-2019-04511) and the Fonds de Recherche Nature et Technologies of  
642 Quebec (2021-PR-283823) that supported this research. H. Huang thanks Yonggang Liu, Jun  
643 Yang and Qiang Wei for hosting her visit at Peking University and assisting her with computing  
644 resources.

645

646

## 647 **References**

- 648 Block, K. and Mauritsen, T.: Forcing and feedback in the MPI - ESM - LR coupled model under  
649 abruptly quadrupled CO<sub>2</sub>, *Journal of Advances in Modeling Earth Systems*, 5, 676-691, 2013.
- 650 Boucher, O., Servonnat, J., Albright, A. L., Aumont, O., Balkanski, Y., Bastrikov, V., Bekki, S.,  
651 Bonnet, R., Bony, S., and Bopp, L.: Presentation and evaluation of the IPSL - CM6A - LR  
652 climate model, *Journal of Advances in Modeling Earth Systems*, 12, e2019MS002010, 2020.
- 653 Bright, R. M. and O'Halloran, T. L.: Developing a monthly radiative kernel for surface albedo  
654 change from satellite climatologies of Earth's shortwave radiation budget: CACK v1. 0, *Geoscientific Model Development*, 12, 3975-3990, 2019.
- 655 Chao, L.-W. and Dessler, A. E.: An assessment of climate feedbacks in observations and climate  
656 models using different energy balance frameworks, *Journal of Climate*, 34, 9763-9773, 2021.
- 657 Collins, W., Ramaswamy, V., Schwarzkopf, M. D., Sun, Y., Portmann, R. W., Fu, Q., Casanova, S.,  
658 Dufresne, J. L., Fillmore, D. W., and Forster, P.: Radiative forcing by well - mixed  
659 greenhouse gases: Estimates from climate models in the Intergovernmental Panel on Climate  
660 Change (IPCC) Fourth Assessment Report (AR4), *Journal of Geophysical Research:  
661 Atmospheres*, 111, 2006.
- 662 Colman, R. and McAvaney, B.: A study of general circulation model climate feedbacks determined  
663 from perturbed sea surface temperature experiments, *Journal of Geophysical Research:  
664 Atmospheres*, 102, 19383-19402, 1997.
- 665 Danabasoglu, G., Lamarque, J. F., Bacmeister, J., Bailey, D., DuVivier, A., Edwards, J., Emmons,  
666 L., Fasullo, J., Garcia, R., and Gettelman, A.: The community earth system model version 2  
667 (CESM2), *Journal of Advances in Modeling Earth Systems*, 12, e2019MS001916, 2020.
- 668 Dessler, A. E.: A determination of the cloud feedback from climate variations over the past decade,  
669 *Science*, 330, 1523-1527, 2010.
- 670 Doelling, D. R., Loeb, N. G., Keyes, D. F., Nordeen, M. L., Morstad, D., Nguyen, C., Wielicki, B.  
671 A., Young, D. F., and Sun, M.: Geostationary enhanced temporal interpolation for CERES  
672 flux products, *Journal of Atmospheric and Oceanic Technology*, 30, 1072-1090, 2013.
- 673 Dong, Y., Armour, K. C., Zelinka, M. D., Proistosescu, C., Battisti, D. S., Zhou, C., and Andrews,  
674 T.: Intermodel spread in the pattern effect and its contribution to climate sensitivity in CMIP5  
675 and CMIP6 models, *Journal of Climate*, 33, 7755-7775, 2020.
- 676 Donohoe, A., Blanchard-Wrigglesworth, E., Schweiger, A., and Rasch, P. J.: The effect of  
677 atmospheric transmissivity on model and observational estimates of the sea ice albedo  
678 feedback, *Journal of Climate*, 33, 5743-5765, 2020.
- 679 Döscher, R., Acosta, M., Alessandri, A., Anthoni, P., Arsouze, T., Bergman, T., Bernardello, R.,  
680 Boussetta, S., Caron, L.-P., and Carver, G.: The EC-Earth3 Earth system model for the  
681 Coupled Model Intercomparison Project 6, *Geoscientific Model Development*, 15, 2973-3020,  
682 2022.
- 683 Eyring, V., Bony, S., Meehl, G. A., Senior, C. A., Stevens, B., Stouffer, R. J., and Taylor, K. E.:
- 684

685 Overview of the Coupled Model Intercomparison Project Phase 6 (CMIP6) experimental  
686 design and organization, *Geoscientific Model Development*, 9, 1937-1958, 2016.

687 Hersbach, H., Bell, B., Berrisford, P., Hirahara, S., Horányi, A., Muñoz - Sabater, J., Nicolas, J.,  
688 Peubey, C., Radu, R., and Schepers, D.: The ERA5 global reanalysis, *Quarterly Journal of the*  
689 *Royal Meteorological Society*, 146, 1999-2049, 2020.

690 Huang, H. and Huang, Y.: Nonlinear coupling between longwave radiative climate feedbacks,  
691 *Journal of Geophysical Research: Atmospheres*, 126, e2020JD033995, 2021.

692 Huang, H. and Huang, Y.: “Data for ERA5 radiative kernels”, *Mendeley Data*, V2, doi:  
693 10.17632/vmg3s67568.2, 2023

694 Huang, H., Huang, Y., and Hu, Y.: Quantifying the energetic feedbacks in ENSO, *Climate*  
695 *Dynamics*, 56, 139-153, 2021a.

696 Huang, Y. and Wang, Y.: How does radiation code accuracy matter?, *Journal of Geophysical*  
697 *Research: Atmospheres*, 124, 10742-10752, 2019.

698 Huang, Y., Huang, H., and Shakirova, A.: The nonlinear radiative feedback effects in the Arctic  
699 warming, *Frontiers in Earth Science*, 651, 2021b.

700 Huang, Y., Ramaswamy, V., and Soden, B.: An investigation of the sensitivity of the clear - sky  
701 outgoing longwave radiation to atmospheric temperature and water vapor, *Journal of*  
702 *Geophysical Research: Atmospheres*, 112, 2007.

703 Huang, Y., Xia, Y., and Tan, X.: On the pattern of CO<sub>2</sub> radiative forcing and poleward energy  
704 transport, *Journal of Geophysical Research: Atmospheres*, 122, 50578-510593, 2017.

705 Huang, Y., Chou, G., Xie, Y., and Souldard, N.: Radiative control of the interannual variability of  
706 Arctic sea ice, *Geophysical Research Letters*, 46, 9899-9908, 2019.

707 Jonko, A. K., Shell, K. M., Sanderson, B. M., and Danabasoglu, G.: Climate feedbacks in CCSM3  
708 under changing CO<sub>2</sub> forcing. Part I: Adapting the linear radiative kernel technique to  
709 feedback calculations for a broad range of forcings, *Journal of Climate*, 25, 5260-5272, 2012.

710 Kolly, A. and Huang, Y.: The radiative feedback during the ENSO cycle: Observations versus  
711 models, *Journal of Geophysical Research: Atmospheres*, 123, 9097-9108, 2018.

712 Kramer, R. J., Soden, B. J., and Pendergrass, A. G.: Evaluating Climate Model Simulations of the  
713 Radiative Forcing and Radiative Response at Earth’s Surface, *Journal of Climate*, 32, 4089-  
714 4102, 2019a.

715 Kramer, R. J., Matus, A. V., Soden, B. J., and L’Ecuyer, T. S.: Observation - based radiative kernels  
716 from CloudSat/CALIPSO, *Journal of Geophysical Research: Atmospheres*, 124, 5431-5444,  
717 2019b.

718 Mauritsen, T., Bader, J., Becker, T., Behrens, J., Bittner, M., Brokopf, R., Brovkin, V., Claussen,  
719 M., Crueger, T., and Esch, M.: Developments in the MPI - M Earth System Model version  
720 1.2 (MPI - ESM1. 2) and its response to increasing CO<sub>2</sub>, *Journal of Advances in Modeling*  
721 *Earth Systems*, 11, 998-1038, 2019.

722 Mlawer, E. J., Taubman, S. J., Brown, P. D., Iacono, M. J., and Clough, S. A.: Radiative transfer  
723 for inhomogeneous atmospheres: RRTM, a validated correlated - k model for the longwave,  
724 *Journal of Geophysical Research: Atmospheres*, 102, 16663-16682, 1997.

725 Myhre, G., Kramer, R., Smith, C., Hodnebrog, Ø., Forster, P., Soden, B., Samset, B., Stjern, C.,  
726 Andrews, T., and Boucher, O.: Quantifying the importance of rapid adjustments for global  
727 precipitation changes, *Geophysical Research Letters*, 45, 11399-311405, 2018.

728 Pendergrass, A. G. and Hartmann, D. L.: The atmospheric energy constraint on global-mean  
729 precipitation change, *Journal of climate*, 27, 757-768, 2014.

730 Pendergrass, A. G., Conley, A., and Vitt, F. M.: Surface and top-of-atmosphere radiative feedback

731 kernels for CESM-CAM5, *Earth System Science Data*, 10, 317-324, 2018.

732 Pincus, R., Buehler, S. A., Brath, M., Crevoisier, C., Jamil, O., Franklin Evans, K., Manners, J.,  
733 Menzel, R. L., Mlawer, E. J., and Paynter, D.: Benchmark calculations of radiative forcing by  
734 greenhouse gases, *Journal of Geophysical Research: Atmospheres*, 125, e2020JD033483,  
735 2020.

736 Previdi, M.: Radiative feedbacks on global precipitation, *Environmental Research Letters*, 5,  
737 025211, 2010.

738 Riihelä, A., Bright, R. M., and Anttila, K.: Recent strengthening of snow and ice albedo feedback  
739 driven by Antarctic sea-ice loss, *Nature Geoscience*, 14, 832-836, 2021.

740 Shell, K. M., Kiehl, J. T., and Shields, C. A.: Using the radiative kernel technique to calculate  
741 climate feedbacks in NCAR's Community Atmospheric Model, *Journal of Climate*, 21, 2269-  
742 2282, 2008.

743 Smith, C. J., Kramer, R. J., and Sima, A.: The HadGEM3-GA7. 1 radiative kernel: the importance  
744 of a well-resolved stratosphere, *Earth System Science Data*, 12, 2157-2168, 2020.

745 Soden, B. J. and Held, I. M.: An assessment of climate feedbacks in coupled ocean-atmosphere  
746 models, *Journal of climate*, 19, 3354-3360, 2006.

747 Soden, B. J., Held, I. M., Colman, R., Shell, K. M., Kiehl, J. T., and Shields, C. A.: Quantifying  
748 climate feedbacks using radiative kernels, *Journal of Climate*, 21, 3504-3520, 2008.

749 Taylor, K. E., Stouffer, R. J., and Meehl, G. A.: An overview of CMIP5 and the experiment design,  
750 *Bulletin of the American meteorological Society*, 93, 485-498, 2012.

751 Thorsen, T. J., Kato, S., Loeb, N. G., and Rose, F. G.: Observation-based decomposition of  
752 radiative perturbations and radiative kernels, *Journal of climate*, 31, 10039-10058, 2018.

753 Vargas Zeppetello, L., Donohoe, A., and Battisti, D.: Does surface temperature respond to or  
754 determine downwelling longwave radiation?, *Geophysical Research Letters*, 46, 2781-2789,  
755 2019.

756 Vial, J., Dufresne, J.-L., and Bony, S.: On the interpretation of inter-model spread in CMIP5  
757 climate sensitivity estimates, *Climate Dynamics*, 41, 3339-3362, 2013.

758 Voldoire, A., Saint - Martin, D., Sénési, S., Decharme, B., Alias, A., Chevallier, M., Colin, J., Gu  
759 érémy, J. F., Michou, M., and Moine, M. P.: Evaluation of CMIP6 deck experiments with  
760 CNRM - CM6 - 1, *Journal of Advances in Modeling Earth Systems*, 11, 2177-2213, 2019.

761 Wetherald, R. and Manabe, S.: Cloud feedback processes in a general circulation model, *Journal*  
762 *of the Atmospheric Sciences*, 45, 1397-1416, 1988.

763 Williams, K., Copsey, D., Blockley, E., Bodas - Salcedo, A., Calvert, D., Comer, R., Davis, P.,  
764 Graham, T., Hewitt, H., and Hill, R.: The Met Office global coupled model 3.0 and 3.1 (GC3.  
765 0 and GC3. 1) configurations, *Journal of Advances in Modeling Earth Systems*, 10, 357-380,  
766 2018.

767 Yue, Q., Kahn, B. H., Fetzer, E. J., Schreier, M., Wong, S., Chen, X., and Huang, X.: Observation-  
768 based longwave cloud radiative kernels derived from the A-Train, *Journal of Climate*, 29,  
769 2023-2040, 2016.

770 Zelinka, M. D., Klein, S. A., and Hartmann, D. L.: Computing and partitioning cloud feedbacks  
771 using cloud property histograms. Part I: Cloud radiative kernels, *Journal of Climate*, 25, 3715-  
772 3735, 2012.

773 Zelinka, M. D., Myers, T. A., McCoy, D. T., Po - Chedley, S., Caldwell, P. M., Ceppi, P., Klein, S.  
774 A., and Taylor, K. E.: Causes of higher climate sensitivity in CMIP6 models, *Geophysical*  
775 *Research Letters*, 47, e2019GL085782, 2020.

776 Zhang, B., Kramer, R. J., and Soden, B. J.: Radiative feedbacks associated with the Madden-Julian

777 oscillation, *Journal of Climate*, 32, 7055-7065, 2019.

778 Zhang, M. and Huang, Y.: Radiative forcing of quadrupling CO<sub>2</sub>, *Journal of Climate*, 27, 2496-  
779 2508, 2014.

780 Zhang, Y., Jin, Z., and Sikand, M.: The top - of - atmosphere, surface and atmospheric cloud  
781 radiative kernels based on ISCCP - H datasets: method and evaluation, *Journal of*  
782 *Geophysical Research: Atmospheres*, 126, e2021JD035053, 2021.

783 Zhou, C., Liu, Y., and Wang, Q.: Calculating the climatology and anomalies of surface cloud  
784 radiative effect using cloud property histograms and cloud radiative kernels, *Advances in*  
785 *Atmospheric Sciences*, 39, 2124-2136, 2022.

786 Zhou, C., Zelinka, M. D., Dessler, A. E., and Yang, P.: An analysis of the short-term cloud feedback  
787 using MODIS data, *Journal of Climate*, 26, 4803-4815, 2013.

788

789

790

791

792

793 **Appendix**

794

795 The ERA5 kernels are computed following Eq. (1) and the approach outlined in Section  
796 2.2.

797

798 1. Surface variable kernels

799

800 To execute the partial radiative perturbation computations, the perturbations are prescribed  
801 as the following: for the 2D feedback variables, the surface temperature is increased by 1 K and  
802 the albedo is increased by 0.01 at each location. Hence, the units of the two kernels,  $K_{TS}$  and  
803  $K_{ALB}$  are  $\text{W m}^{-2} \text{K}^{-1}$  and  $\text{W m}^{-2} \%^{-1}$ , respectively. When applying them to feedback  
804 quantification, their feedbacks are quantified as

805 
$$\Delta R_{TS} = K_{TS} \cdot \Delta T_S \quad (\text{A1})$$

806 
$$\Delta R_{Alb} = K_{ALB} \cdot \Delta Alb \quad (\text{A2})$$

807 where  $\Delta T_S$  should be measured in the units of K and  $\Delta Alb$  in absolute values, i.e., the multiply of  
808 1%.

809

810 2. Water vapor kernel

811

812 For the 3D feedback variables, the perturbations are applied to each of the 37 pressure  
813 layers (from 1hPa to 1000hPa) and one layer at a time. For the water vapor kernel, a 10%  
814 incremental perturbation of the water vapor concentration is used. To adapt to the convention  
815 used in the majority of the existing kernels, we convert the units of the kernels to represent the  
816 radiative flux change corresponding to an increase of water vapor concentration that conserves  
817 the relative humidity of the layer under a 1-K increase in air temperature, i.e., converting the  
818 units from  $\text{W}/(\text{m}^2 \Delta q_0^{+10\%} 100\text{hPa})$  to  $\text{W}/(\text{m}^2 \Delta q_0^{+1K} 100\text{hPa})$ :

819 
$$K_q^{+10\%} = \frac{\Delta R_0}{\Delta q_0^{+10\%}} \quad (\text{A3})$$

820 
$$K_q^{+1K} = \frac{\Delta R_0}{\Delta q_0^{+1K}} = K_q^{+10\%} \cdot \frac{\Delta q_0^{+10\%}}{\Delta q_0^{+1K}} = K_q^{+10\%} \cdot \frac{\Delta q_0^{+10\%}}{q_0} \cdot \frac{e_s(T_0)}{e_s(T_0+1K) - e_s(T_0)} \quad (\text{A4})$$

821 Where  $q_0$  is the unperturbed water vapor concentration, in units of  $\text{kg kg}^{-1}$ .  $\Delta q_0^{+10\%}$  is a 10%  
822 increment in water vapor concentration.  $e_s(T)$  is the saturated water vapor pressure under  
823 temperature  $T$ , and can be measured by empirical formulas; hence,  $\Delta q_0^{+1K}$  can be measured as  
824  $q_0 \left[ \frac{e_s(T_0+1K)}{e_s(T_0)} - 1 \right]$ . Accordingly, when the water vapor kernel is used for water vapor feedback  
825 quantification, the feedback is measured as:

826 
$$\Delta R_q = K_q^{+1K} \cdot \Delta q^{+1K} = K_q^{+1K} \cdot \frac{\Delta q}{\Delta q_0^{+1K}} = K_q^{+1K} \cdot \frac{\Delta q}{q_0} \cdot \frac{e_s(T_0)}{e_s(T_0+1K) - e_s(T_0)} \quad (\text{A5})$$

827 where  $\Delta q = q - q_0$  measures the change in water vapor concentration and is normalized by  
828  $\Delta q_0^{+1K}$  to give the factor that is multipliable with the  $K_q^{+1K}$  kernel value. If using the Clapeyron-  
829 Clausius relation, the above expression can be further approximated as

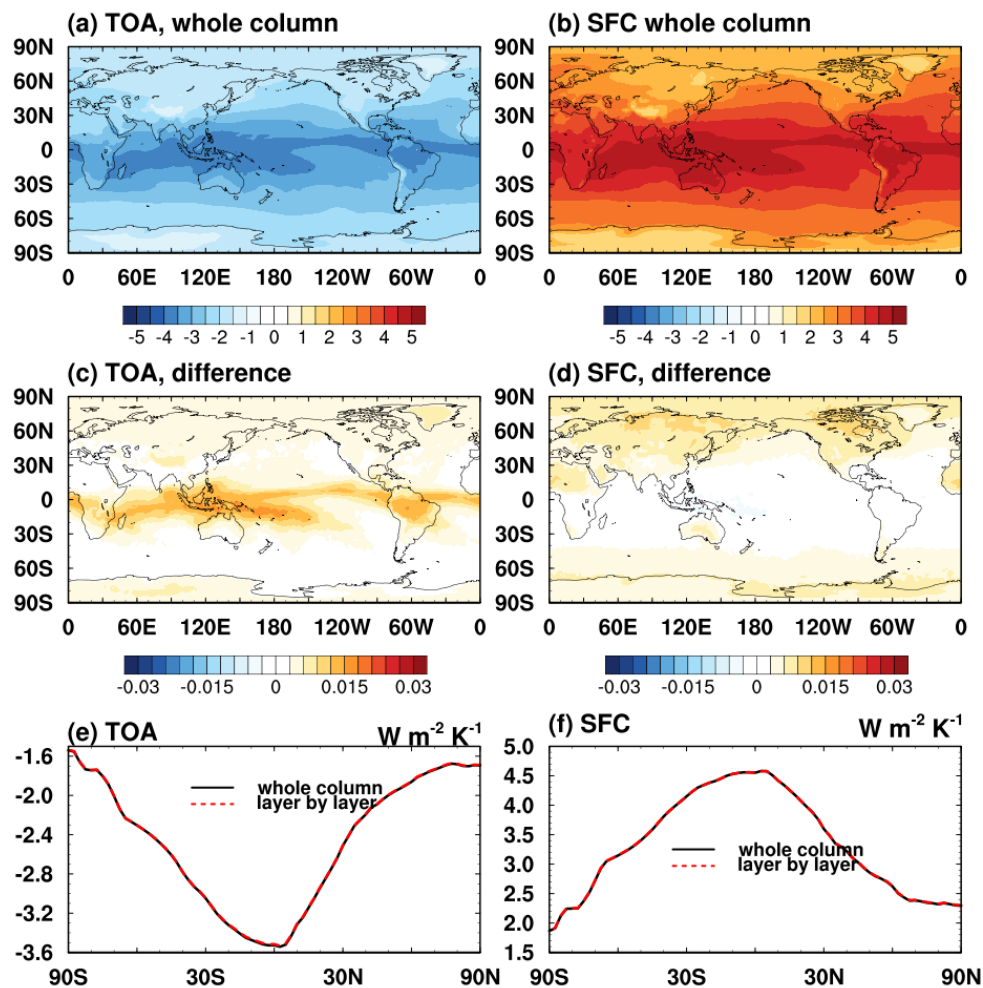
830 
$$\Delta R_q = K_q^{+1K} \cdot \frac{\Delta q}{q_0} \cdot \frac{e_s}{(de_s/dT) \cdot 1K} = K_q^{+1K} \cdot \frac{\Delta q}{q_0} \cdot \frac{R_v}{L_v} \cdot \frac{T_0^2}{1K} \quad (\text{A6})$$

831 where  $R_v$  and  $L_v$  are the gas constant and specific latent heat of water vapor, respectively. Note  
832 that when the kernels are used,  $T_0$  and  $q_0$  typically take their values from the base climate  
833 appropriate to the application, e.g., the unperturbed climate of a GCM experiment, not  
834 necessarily the dataset used for kernel computation.

835  
836 3. Air temperature kernel

837  
838 For the air temperature kernel, to be consistent with the “inhomogeneous path treatment”  
839 that accounts for the vertically non-uniform temperature distribution within each discrete  
840 atmospheric layer (Mlawer et al., 1997), perturbations are added not only to the layer-mean  
841 temperature but also the temperature at the exiting boundary of radiative fluxes of interest (i.e.,  
842 the upper boundary of each layer for the TOA flux and the lower boundary for the surface flux),  
843 to appropriately represent the physical temperature perturbation in each layer.

844 A meaningful test to affirm the validity of the air temperature kernel is a vertical sum test,  
845 i.e., a linear additivity test to verify the vertical integration of the kernel values reproduce the  
846 flux change, either at TOA or surface, in response to a whole-column air temperature increase of  
847 1K. Figure A1 shows that the ERA5 kernel well passes this test. However, as shown by Figure 9,  
848 some kernels (e.g., HadGEM3 kernel) show much weaker radiative response at surface, possibly  
849 due to improper treatment of the air temperature perturbation in the kernel computation, which  
850 may lead to an underestimated air temperature feedback and large biases in the surface feedback  
851 analysis.  
852

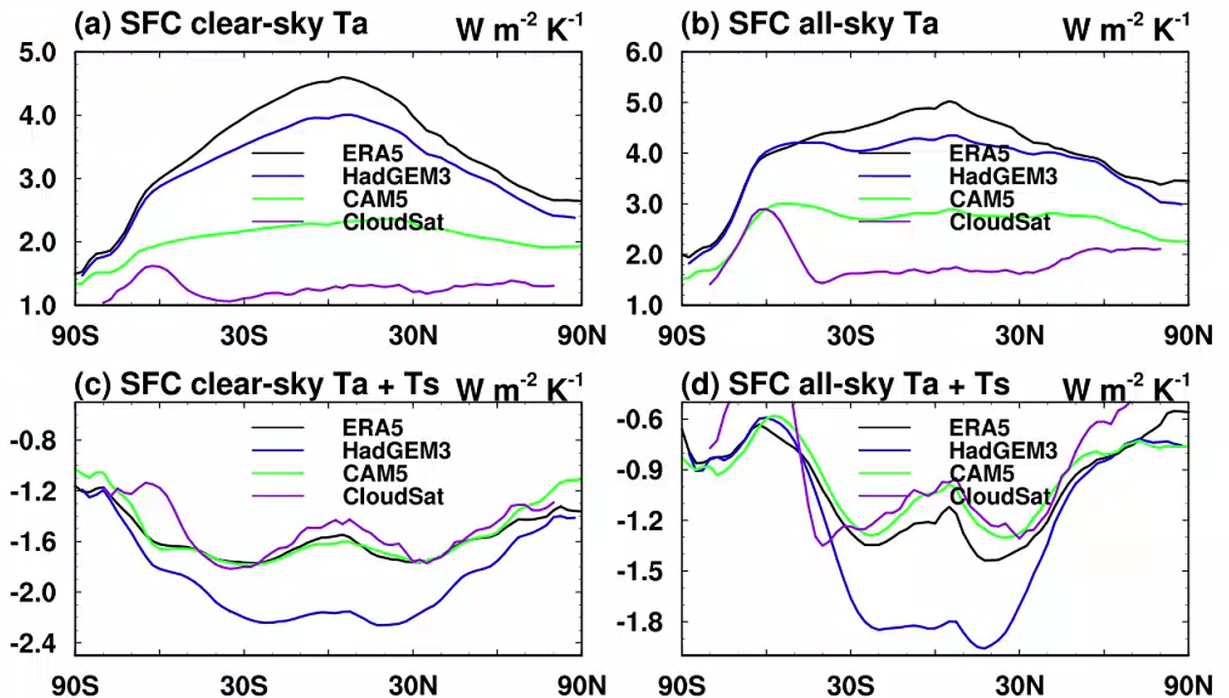


853

854 Figure A1. Monthly mean TOA and surface radiation flux change in response to a +1K  
 855 air temperature perturbation throughout the vertical column: (a, b) computed by a radiation  
 856 model, RRTMG; (c, d) difference of vertical sum of air temperature kernels compared to truth in  
 857 (a, b); (e, f) comparison of the zonal mean.

858

859 Another challenge in the computation of air temperature kernel for surface flux is that the  
 860 surface in radiative transfer models is also the lower boundary of the lowermost atmospheric  
 861 layer. If the effects of the surface temperature perturbation on the emission of the surface and  
 862 that of the lowermost atmospheric layer are not distinguished, this may lead to improper  
 863 interpretation and use of the surface temperature kernel. In our ERA5 kernel, the two effects are  
 864 considered separately: according to radiative transfer theory, an increase in surface skin  
 865 temperature only affects the surface upward emission; an increase in air temperature only affects  
 866 the downward radiation. In some other kernels such as CAM5, these effects are not  
 867 distinguished, so that the kernel value represents the net effect, i.e., change in the sum of both  
 868 downward and upward. As a result, in Table S4, we can only report the sum of surface and air  
 869 temperature feedbacks. Figure A2 shows the comparison of vertically integrated air temperature  
 870 kernels and the sum of surface and air temperature kernels between ERA5, CAM5, HadGEM3  
 871 and CloudSat. Although the strength of vertically integrated air temperature kernel for CAM5 is  
 872 much weaker than that for ERA5 (Figure A2a and b), the sum of surface and air temperature  
 873 kernel between these two datasets are in good agreement (Figure A2c and d), which warns that  
 874 the seemingly right temperature feedback quantified by some kernels might come from the  
 875 misattribution of surface temperature contributions. Another noticeable feature in Figure A2 is  
 876 that the HadGEM3 kernel shows an underestimation in vertical integration of air temperature  
 877 kernel and an overestimation in the sum of surface and air temperature kernel, likely due to  
 878 mistreatment of the bottom layer, and this accounts for the biased surface feedback analysis as  
 879 shown in Figure 9. Similar issues were noticed in Kramer et al. (2019a).



880

881 Figure A2. Comparison of annual mean surface kernels for ERA5, CAM5, CloudSat and  
 882 HadGEM3 for (a, b) the vertically integrated air temperature kernel values, and (c, d) sum of  
 883 surface and air temperature kernels.  
 884  
 885

886 4. Time averaging  
 887

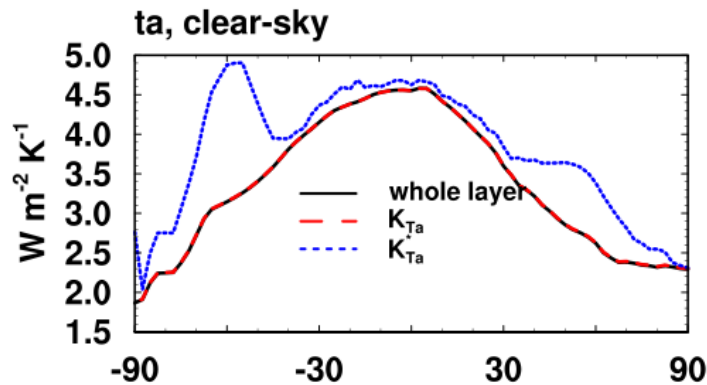
888 As described in Section 2.2, all the kernels provided for feedback analysis are averaged  
 889 from instantaneous kernel values over each calendar month and, in the ERA5 kernel, over  
 890 multiple years. This is to ensure proper sampling of radiative sensitivity values under different  
 891 atmospheric states, so that the kernels are representative of mean radiative sensitivity and thus  
 892 can be readily multiplied with monthly mean climate responses ( $\Delta X$ ) to evaluate climate  
 893 feedbacks.

894 If the kernels are computed for fixed pressure levels, and if the pressure of any of these  
 895 levels of an instantaneous atmospheric profile is higher than the surface pressure (i.e., the level is  
 896 below the surface) at a time instance, this potentially creates inconsistency in the averaging  
 897 procedure. To address this concern, we set the kernel value to zero (as opposed to missing value)  
 898 before averaging. This is to ensure that when multiplied with the monthly mean climate response  
 899 ( $\Delta X$ ), the contribution of a pressure layer (e.g., that centered at 1000 hPa) is effectively counted  
 900 only for the fraction of time the layer exists (when surface pressure is higher than 1000 hPa).  
 901 Otherwise, the feedback quantification needs to be further weighted with fraction of time ( $f$ )  
 902 when the pressure layer exists. For example, if the surface pressure is larger than 1000hPa only  
 903 for half of time in a month ( $f=0.5$ ), the radiation flux anomaly contributed by the layer centered  
 904 at 1000 hPa is:

905  
 906 
$$\Delta R_{T_{1000hPa}} = K_{T_{1000hPa}}^* \cdot \Delta T_{1000hPa} \cdot f \quad (A7)$$
  
 907

908 Here,  $K_{T_{1000hPa}}^*$  represents the kernel value averaged from the time instances when the layer  
 909 exists. Our averaging scheme is essentially to provide a kernel  $K_{T_{1000hPa}} = K_{T_{1000hPa}}^* \cdot f$ , so that  
 910 it can be simply multiplied with  $\Delta T_{1000hPa}$  to obtain the same result.

911 Figure A3 illustrates the differences between  $K_{T_a}^*$  and  $K_{T_a}$ , in terms of their vertically  
 912 integrated value. Such difference is pronounced over the Southern Oceans (around 60S), where  
 913 the surface pressure value varies considerably. This likely explains why Figure 3h shows  
 914 noticeable differences in the air temperature kernel in this region.



915



916 Figure A3. Zonal mean monthly mean air temperature kernels for surface flux from  
917 ERA5 in clear-sky. Black line is the result from the whole column perturbation computation by  
918 RRTMG, providing a "truth" for comparison. Red dashed line is the kernel weighted with  
919 fraction of time ( $K_{T_a}$ ) and blue dotted line represents results without weights ( $K_{T_a}^*$ ).

920

## 921 5. Layer-specified and layer thickness-normalized radiative kernels

922

923 We generate two versions of vertically resolved air temperature kernel, water vapor LW  
924 and SW kernel, one with values corresponding to specified vertical layers, i.e., in the units of  $\text{W}$   
925  $\text{m}^{-2} \text{K}^{-1}$ , and another with unit-layer thickness (e.g., as shown in Figure 2 and 4), i.e., in  $\text{W m}^{-2} \text{K}^{-1}$   
926  $100\text{hPa}^{-1}$ . The latter one properly portrays the vertical distribution of radiative sensitivity to  
927 perturbations in unit thickness layers, while the former one may be more convenient to use in  
928 feedback quantifications. For TOA budget analyses, these two versions of kernels lead to little  
929 difference in practice due to limited contributions from the bottom atmospheric layer. However,  
930 for surface budget analyses, we recommend using the layer-specified kernels, as the surface  
931 kernels typically show strongest sensitivity to the perturbations in the bottom layers, which can  
932 be best accounted for in the non-normalized kernels. Otherwise, the difference of surface  
933 pressure between ERA5 and GCMs needs to be carefully treated to avoid errors, for example,  
934 caused by missing the radiative contribution from the bottom layer of the atmosphere.

935

936

937

938

939